

New fixed-target experiments to search for dark gauge forcesJames D. Bjorken,¹ Rouven Essig,¹ Philip Schuster,¹ and Natalia Toro²¹*Theory Group, SLAC National Accelerator Laboratory, Menlo Park, California 94025, USA*²*Theory Group, Stanford University, Stanford, California 94305, USA*

(Received 20 July 2009; published 28 October 2009)

Fixed-target experiments are ideally suited for discovering new MeV–GeV mass $U(1)$ gauge bosons through their kinetic mixing with the photon. In this paper, we identify the production and decay properties of new light gauge bosons that dictate fixed-target search strategies. We summarize existing limits and suggest five new experimental approaches that we anticipate can cover most of the natural parameter space, using currently operating GeV-energy beams and well-established detection methods. Such experiments are particularly timely in light of recent terrestrial and astrophysical anomalies (PAMELA, Fermi, DAMA/LIBRA, etc.) consistent with dark matter charged under a new gauge force.

DOI: 10.1103/PhysRevD.80.075018

PACS numbers: 14.70.Pw, 95.35.+d

I. NEW GAUGE FORCES

The interactions of ordinary matter establish that three gauge forces survive to low energies. Two striking features of these forces—electroweak symmetry breaking at a scale far below the Planck scale and apparent unification assuming low-energy supersymmetry—have driven model building for a quarter century. But the strong and electroweak forces need not be the only ones propagating at long distances. Additional forces, under which ordinary matter is neutral, would have gone largely unnoticed because gauge symmetry prohibits renormalizable interactions between standard model fermions and the other “dark” gauge bosons or matter charged under them.

There is an important exception to the above claim: new dark Abelian forces can couple to the standard model hypercharge through the kinetic mixing operator $\frac{\epsilon}{2} F_{\mu\nu}^Y F'^{\mu\nu}$, where $F'_{\mu\nu} = \partial_{[\mu} A'_{\nu]}$ and A' is the dark gauge field [1]. If the A' is massive, standard model matter acquires millicharges proportional to ϵ under the massive A' . Kinetic mixing with $\epsilon \sim 10^{-8}$ – 10^{-2} can be generated at any scale by loops of heavy fields charged under both $U(1)'$ and $U(1)_Y$, and the A' can acquire mass through a technicolor, Higgs, or Stueckelberg mechanism (from string theory, the possible range of ϵ is much larger, namely, 10^{-23} – 10^{-2} [2–5]). A mass scale near but beneath the weak scale is particularly well motivated— $U(1)'$ symmetry breaking may be protected by the same physics that stabilizes the electroweak hierarchy [6]. Indeed, if the largest symmetry-breaking effects arise from weak-scale supersymmetry breaking, then the $U(1)'$ symmetry-breaking scale is naturally suppressed by a loop factor or by $\sqrt{\epsilon}$, leading to MeV- to GeV-scale A' masses [2,6–10].

An A' can be produced in collisions of charged particles with nuclei and can decay to electrons or muons. The production cross section ($\sigma_{A'}$) and decay length ($\gamma c\tau$),

$$\sigma_{A'} \sim 100 \text{ pb} (\epsilon/10^{-4})^2 (100 \text{ MeV}/m_{A'})^2, \quad (1)$$

$$\gamma c\tau \sim 1 \text{ mm} (\gamma/10) (10^{-4}/\epsilon)^2 (100 \text{ MeV}/m_{A'}), \quad (2)$$

vary by 10 orders of magnitude for the ϵ 's and masses $m_{A'}$ we consider. This wide range calls for multiple experimental approaches, with different strategies for confronting backgrounds. Beam-dump searches from the 1980s exclude the low-mass and small- ϵ parameter range, and other data constrain large ϵ . In this paper we suggest five scenarios for fixed-target experiments sensitive to distinct but overlapping regions of parameter space (see Fig. 1). Together they can probe six decades in A' coupling and three decades in A' mass with existing beam energies and intensities.

Dark matter interpretations of recent astrophysical and terrestrial anomalies provide a further impetus to search for new $U(1)'$'s. Annihilation of dark matter charged under a new $U(1)'$ into the A' can explain the electron and/or positron excesses observed by PAMELA [11], ATIC [12], Fermi [13], and HESS [14,15] (see e.g. [16–23]). If the dark matter is also charged under a non-Abelian group, then its spectrum naturally implements an inelastic dark matter scenario [24], thereby explaining the annual modulation signal reported by DAMA/LIBRA [25,26] and reconciling it with the null results of other experiments [16,24,27,28]. Several decaying dark matter scenarios also make use of a hidden sector [29–33].

In view of these suggestive data and the abundant theoretical speculation surrounding them, insight from new experiments is clearly called for. New probes of weakly mixed MeV–GeV $U(1)'$'s directly probe the low-energy structure of these scenarios, where the nature of their interactions is most manifest. As such, the experiments we advocate here are complementary to upcoming gamma-ray observations (see e.g. [34,35]) and to the next generation of direct detection experiments [36–40] that will shed light on the scattering of dark matter.

A. Direct tests of low-mass gauge sectors

Constraints on new A' 's and the reach of different experiments are summarized in Fig. 1. To begin, low-energy e^+e^- colliders are a powerful laboratory for the study of an

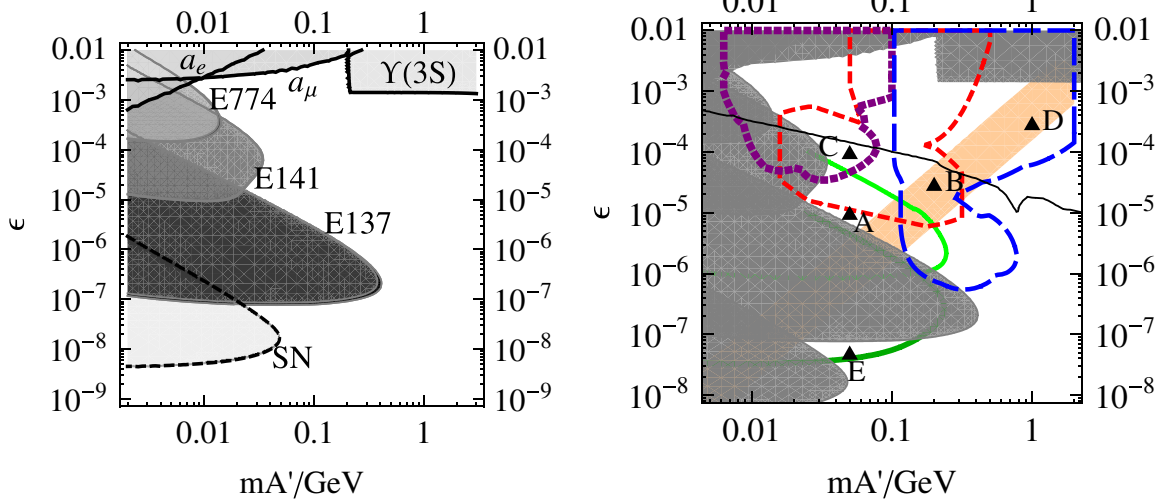


FIG. 1 (color online). *Left:* Existing constraints on an A' . Shown are constraints from electron and muon anomalous magnetic moment measurements, a_e and a_μ , the *BABAR* search for $Y(3S) \rightarrow \gamma\mu^+\mu^-$, three beam-dump experiments, E137, E141, and E774, and supernova cooling (SN). These constraints are discussed further in Sec. III. *Right:* Existing constraints are shown in gray, while the various lines—light green (upper) solid, red short-dashed, purple dotted, blue long-dashed, and dark green (lower) solid—show estimates of the regions that can be explored with the experimental scenarios discussed in Secs. IV A, IV B, IV C, IV D, and IV E, respectively. The discussion in Sec. IV focuses on the five points labeled “A” through “E.” The orange stripe denotes the “D-term” region introduced in Sec. II A, in which simple models of dark matter interacting with the A' can explain the annual modulation signal reported by DAMA/LIBRA. Along the thin black line, the A' proper lifetime $c\tau = 80 \mu\text{m}$, which is approximately the τ proper lifetime—see Eq. (11).

A' with $\epsilon \gtrsim 10^{-4}$ and mass above ~ 200 MeV, particularly in sectors with multiple light states [41–45]. Their reach in ϵ is limited by luminosity and irreducible backgrounds. However, an A' can also be produced through bremsstrahlung off an electron beam incident on a fixed target [43]. This approach has several virtues over colliding-beam searches: much larger luminosities, of $\mathcal{O}(1 \text{ ab}^{-1}/\text{day})$, can be achieved, scattering cross sections are enhanced by nuclear charge coherence, and the resulting boosted final states can be observed with compact special-purpose detectors.

Past electron “beam-dump” experiments, in which a detector looks for decay products of rare penetrating particles behind a stopped electron beam, constrain $\gtrsim 10$ cm vertex displacements and $\epsilon \gtrsim 10^{-7}$. The thick shield needed to stop beam products limits these experiments to long decay lengths, so thinner targets are needed to probe shorter displacements (larger ϵ and $m_{A'}$). However, beam products easily escape thin targets and constitute a challenging background in downstream detectors.

The five benchmark points labeled “A” through “E” in Fig. 1 (right) require different approaches to these challenges, discussed in Sec. IV. We have estimated the reach of each scenario, summarized in Fig. 1 (right), in the context of electron beams with 1–6 GeV energies, nA– μ A average beam currents, and run times $\sim 10^6$ s. Such beams can be found, for example, at the Thomas Jefferson National Accelerator Facility (JLab), the SLAC National Accelerator Laboratory, the electron accelerator ELSA, and the Mainzer Mikrotron (MAMI).

The scenarios for points A and E use 100 MeV–1 GeV electron beam dumps, with more complete event reconstruction or higher-current beams than previous dump experiments. Low-mass, high- ϵ regions (e.g. B and C) produce boosted A' and forward decay products with mm–cm displaced vertices. Our approaches exploit very forward silicon-strip tracking to identify these vertices, while maintaining reasonable occupancy—a limiting factor. At still higher ϵ , no displaced vertices are resolvable and one must take full advantage of the kinematic properties of the signal and background processes, including the recoiling electron, using either the forward geometries of B and C or a wider-angle spectrometer (e.g. for point D). Spectrometers operating at various laboratories appear capable of probing this final region. Table I summarizes the various experimental scenarios.

We focus on the case where the A' decays directly to standard model fermions, but the past experiments and proposed scenarios are also sensitive (with different exclusions) if the A' decays to lighter $U(1)'$ -charged scalars, and to direct production of axionlike states.

B. Outline

In Sec. II, we summarize the properties of A' production through bremsstrahlung in fixed-target collisions. Constraints from past experiments and from neutrino emission by SN 1987A are presented in Sec. III. In Sec. IV, we describe the five new experimental scenarios and estimate the limiting backgrounds. We conclude in Sec. V with a

TABLE I. Summary of suggested experimental scenarios and benchmark points—see Sec. IV for more details. For the five experimental scenarios, we show the mass, ϵ , beam energy (E_{beam}), decay length ($\gamma c\tau$), length of the target, shield, and detector region, visibility of a vertex, dominant background, and rough amount of charge that needs to be dumped to yield at least 10 events in a sizeable region of parameter space around the benchmark point. For the “vertex visible?” row, “yes*” means that requiring a vertex allows the region around the indicated benchmark point to be probed, but that a significant (and different) parameter region with higher ϵ can also be probed without using a vertex but assuming very good mass resolution (see subsection within Sec. IV D). For the dominant background row, “tridents” refers to the QED tridents shown in Fig. 3, while “occupancy” refers to limitations imposed by the silicon tracking elements.

Benchmark	A (Sec. IV A)	B (Sec. IV B)	C (Sec. IV C)	D (Sec. IV D)	E (Sec. IV E)
$m_{A'}$ (MeV)	50	200	50	1000	50
ϵ	10^{-5}	3×10^{-5}	10^{-4}	3×10^{-4}	5×10^{-8}
E_{beam} (GeV)	0.2	6	1	4	0.2
$\gamma c\tau$ (cm)	6.4	1.4	0.3	3.6×10^{-4}	2.6×10^5
Target/shield/detector (cm)	10/10/30	0.3/none/100	0.3/none/100	0.3/none/100	30/500/500
Vertex visible?	Yes	Yes*	Yes*	No	Yes
Dominant background	Beam remnants	Tridents/occupancy	Occupancy	Tridents/occupancy	None
Charge dumped (C)	0.1	$10^{-3} - 0.1$	10^{-5}	100	5000

summary of the prospects for new experiments. More detailed formulas, which we use to calculate our expected search reaches, and a more detailed discussion of some of the backgrounds, are given in Appendixes A, B, and C.

II. THE PHYSICS OF NEW $U(1)$ VECTORS IN FIXED-TARGET COLLISIONS

A. Theoretical preliminaries

Consider the Lagrangian

$$\mathcal{L} = \mathcal{L}_{\text{SM}} + \epsilon_Y F^{Y,\mu\nu} F'_{\mu\nu} + \frac{1}{4} F'^{\mu\nu} F'_{\mu\nu} + m_{A'}^2 A'^{\mu} A'_{\mu}, \quad (3)$$

where \mathcal{L}_{SM} is the standard model Lagrangian, $F'_{\mu\nu} = \partial_{[\mu} A'_{\nu]}$, and A' is the gauge field of a massive dark $U(1)'$ gauge group [1]. The second term in (3) is the kinetic mixing operator, and $\epsilon \sim 10^{-8} - 10^{-2}$ is naturally generated by loops at any mass scale of heavy fields charged under both $U(1)'$ and $U(1)_Y$; the lower end of this range is obtained if one or both $U(1)$'s are contained in grand-unified groups, since then ϵ is only generated by two- or three-loop grand-unified-breaking effects.

A simple way of analyzing the low-energy effects of the A' is to treat kinetic mixing as an insertion of $p^2 g_{\mu\nu} - p_{\mu} p_{\nu}$ in Feynman diagrams, making it clear that the A' couples to the electromagnetic current of the standard model through the photon. This picture also clarifies, for example, that new interactions induced by kinetic mixing must involve a massive A' propagator, and that effects of mixing with the Z boson are further suppressed by $1/m_Z^2$. Equivalently, one can redefine the photon field $A^{\mu} \rightarrow A^{\mu} + \epsilon A'^{\mu}$ as in [10], which removes the kinetic mixing term and generates a coupling $e A_{\mu} J_{\text{EM}}^{\mu} \supset \epsilon e A'_{\mu} J_{\text{EM}}^{\mu}$ of the new gauge boson to electrically charged particles (here $\epsilon \equiv \epsilon_Y \cos\theta_W$). Note that this does not induce electromag-

netic millicharges for particles charged under the A' . The parameters of concern in this paper are ϵ and $m_{A'}$.

We now explain the orange stripe in Fig. 1—see [2,7,8] for more details. In a supersymmetric theory, the kinetic mixing operator induces a mixing between the D -terms associated with $U(1)'$ and $U(1)_Y$. The hypercharge D -term gets a vacuum expectation value from electroweak symmetry breaking and induces a weak-scale effective Fayet-Iliopoulos term for $U(1)'$. Consequently, the standard model vacuum can break the $U(1)'$ in the presence of light $U(1)'$ -charged degrees of freedom, giving the A' a mass,

$$m_{A'} \sim \sqrt{\epsilon g_D} \frac{\sqrt{g_Y} m_W}{g_2}, \quad (4)$$

where g_D , g_Y , and g_2 are the $U(1)'$, $U(1)_Y$, and standard model $SU(2)_L$ gauge couplings, respectively, and m_W is the W -boson mass. Equation (4) relates ϵ and $m_{A'}$ as indicated by the orange stripe in Fig. 1 for $g_D \sim 0.1 - 1$. This region is not only theoretically appealing, but also roughly corresponds to the region in which the annual modulation signal observed by DAMA/LIBRA can be explained by dark matter, charged under the $U(1)'$, scattering inelastically off nuclei through A' exchange. We therefore include these lines for reference in our plots.

B. A' production in fixed-target collisions

A' particles are generated in electron collisions on a fixed target by a process analogous to ordinary photon bremsstrahlung (see Fig. 2). This can be reliably estimated in the Weizsäcker-Williams approximation (see Appendix A for more details) [46–48]. When the incoming electron has energy E_0 , the differential cross section to produce an A' of mass $m_{A'}$ with energy $E_{A'} \equiv x E_0$ is

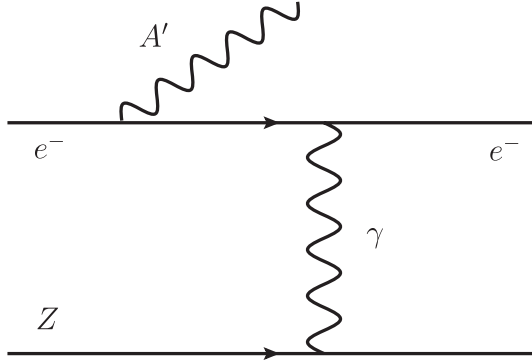


FIG. 2. A' production by bremsstrahlung off an incoming electron scattering off protons in a target with atomic number Z .

$$\frac{d\sigma}{dx d\cos\theta_{A'}} \approx \frac{8Z^2\alpha^3\epsilon^2 E_0^2 x}{U^2} \mathcal{L}og \times \left[\left(1 - x + \frac{x^2}{2}\right) - \frac{x(1-x)m_{A'}^2(E_0^2 x \theta_{A'}^2)}{U^2} \right], \quad (5)$$

where Z is the atomic number of the target atoms, $\alpha \approx 1/137$, $\theta_{A'}$ is the angle in the lab frame between the emitted A' and the incoming electron, the $\mathcal{L}og$ (~ 5 – 10 for $m_{A'} \lesssim 500$ MeV) depends on kinematics, atomic screening, and nuclear size effects (see Appendix A and Fig. 10 therein), and

$$U(x, \theta_{A'}) = E_0^2 x \theta_{A'}^2 + m_{A'}^2 \frac{1-x}{x} + m_e^2 x \quad (6)$$

is the virtuality of the intermediate electron in initial-state bremsstrahlung. The above results are valid for

$$m_e \ll m_{A'} \ll E_0, \quad x\theta_{A'}^2 \ll 1. \quad (7)$$

Dropping m_e and performing the angular integral, we find

$$\frac{d\sigma}{dx} \approx \frac{8Z^2\alpha^3\epsilon^2 x}{m_{A'}^2} \left(1 + \frac{x^2}{3(1-x)}\right) \mathcal{L}og. \quad (8)$$

The x -scaling and singularity structure $\frac{\alpha^3}{m_e^2 x}$ of massless bremsstrahlung [48] is recovered from (5) with $m_{A'}^2 = 0$ (the polynomial factor differs because of finite $m_{A'}$ corrections to the matrix element), but differs from the massive A' -strahlung in several important ways. We emphasize that these properties are not particular to any matrix element, but instead are kinematic properties common to all heavy-particle emission:

Rate: For most x , $U(x, 0) \sim m_{A'}^2$, so that the total A' production rate is controlled by $\frac{\alpha^3 \epsilon^2}{m_{A'}^2}$. Therefore, it is suppressed relative to photon bremsstrahlung by $\sim \epsilon^2 (m_e^2/m_{A'}^2)$.

Energy: A' bremsstrahlung is sharply peaked at $x \approx 1$, where $U(x, 0)$ is minimized. When an A' is produced, it carries nearly the entire beam energy—in fact the median value of $(1-x)$ is $\sim \max\left(\frac{m_e}{m_{A'}}, \frac{m_{A'}}{E_0}\right)$.

Angle: A' emission is dominated at angles $\theta_{A'}$ such that $U(x, \theta_{A'}) \lesssim 2U(x, 0)$ (beyond this point, wide-angle emission falls as $1/\theta_{A'}^4$). For x near its median value, the cutoff emission angle is

$$\theta_{A' \text{ max}} \sim \max\left(\frac{\sqrt{m_{A'} m_e}}{E_0}, \frac{m_{A'}^{3/2}}{E_0^{3/2}}\right), \quad (9)$$

which is parametrically smaller than the opening angle of the A' decay products, $\sim m_{A'}/E_0$. The approximation of collinear emission is justified in many calculations.

Because these features apply to bremsstrahlung of any massive boson, there is a simple approximate equivalence between constraints on the A' and constraints on an axion with mass $m_a = m_{A'}$ and decay constant $f_a \sim 1.7 \times 10^{-3} \text{ GeV} c_e / \epsilon$, at least when the constraints come from coupling to electrons. Here the coupling constant of axions to electrons is assumed to be $C_e m_e / f_a$, where C_e is a model-dependent coefficient.

The total number of A' produced when N_e electrons of initial energy E_0 scatter in a target of T radiation lengths is

$$\frac{dN}{dx} = N_e \frac{N_0 X_0}{A} \int_{E_{A'}}^{E_0} \frac{dE_1}{E_1} \times \int_0^T dt I(E_1; E_0, t) E_0 \frac{d\sigma}{dx'} \Big|_{x'=E_{A'}/E_1}, \quad (10)$$

where $x' \equiv E_{A'}/E_1$, X_0 is the radiation length of the target, $N_0 \approx 6 \times 10^{23} \text{ mole}^{-1}$ is Avogadro's number, A is the target atomic mass in g/mole, and I is the energy distribution of electrons after passing through t radiation lengths.

After the A' is produced in the target, it will travel for some distance before decaying back into standard model particles [we will assume throughout this paper that no other decay channels into particles charged under the $U(1)'$ are available]. The proper lifetime of the A' is

$$c\tau = \frac{1}{\Gamma} \approx \frac{3}{N_{\text{eff}} m_{A'} \alpha \epsilon^2} \approx \frac{80 \mu\text{m}}{N_{\text{eff}}} \left(\frac{10^{-4}}{\epsilon}\right)^2 \left(\frac{100 \text{ MeV}}{m_{A'}}\right), \quad (11)$$

where we have neglected phase-space corrections and N_{eff} counts the number of available decay products [$N_{\text{eff}} = 1$ for $m_{A'} \lesssim 2m_\mu$ when only $A' \rightarrow e^+e^-$ decays are possible, and $2 + R(m_{A'})$ for $m_{A'} \geq 2m_\mu$, where R is defined to be the energy dependent ratio $\frac{\sigma(e^+e^- \rightarrow \text{hadrons})}{\sigma(e^+e^- \rightarrow \mu^+\mu^-)}$ [49]]. A' decays will thus create displaced vertices behind the target. While $c\tau$ determines the typical impact parameter for these displaced tracks, their vertex displacements are controlled by (for the typical kinematics with $x \approx 1$)

$$\begin{aligned} \ell_0 &\equiv \gamma c \tau \simeq \frac{3E_1}{N_{\text{eff}} m_{A'}^2 \alpha \epsilon^2} \\ &\simeq \frac{0.8 \text{ cm}}{N_{\text{eff}}} \left(\frac{E_0}{10 \text{ GeV}} \right) \left(\frac{10^{-4}}{\epsilon} \right)^2 \left(\frac{100 \text{ MeV}}{m_{A'}} \right)^2, \end{aligned} \quad (12)$$

where we have again neglected phase-space corrections.

C. Approximate total rate formulas

From Eqs. (8) and (12), we can obtain simple approximate expressions for the rate of A' production in scattering off thin targets (with $T \ll 1$) and thick “dump” targets ($T \gg 1$). These crude approximations are only correct within about 1 order of magnitude, but they are useful in quickly mapping out regions in the large logarithmic parameter space. In our results we use more accurate expressions that also include detector acceptances, as presented in Appendixes A and B.

In the thin-target limit $T \ll 1$, the beam is not significantly degraded as it passes through the target, and $I(E_1, E_0, t) \approx \delta(E_1 - E_0)$. In this case the total A' production rate scales as

$$N \sim N_e \frac{N_0 X_0}{A} T \frac{Z^2 \alpha^3 \epsilon^2}{m_{A'}^2} \mathcal{L} \text{og} = N_e \mathcal{C} T \epsilon^2 \frac{m_e^2}{m_{A'}^2}, \quad (13)$$

where $\mathcal{C} \approx 5$ is only logarithmically dependent on the choice of nucleus (at least in the range of masses where the form factor is only slowly varying) and on $m_{A'}$, because, roughly, $X_0 \propto \frac{A}{Z^2}$ (see Appendix B and [49]). For example, for a Coulomb of incident electrons

$$\frac{N}{\mathcal{C}} \sim 10^6 \left(\frac{T}{0.1} \right) \left(\frac{\epsilon}{10^{-4}} \right)^2 \left(\frac{100 \text{ MeV}}{m_{A'}} \right)^2. \quad (14)$$

For a thick target ($T \gg 1$), production is dominated near the front of the target and

$$N \sim N_e \mathcal{C}' \epsilon^2 \frac{m_e^2}{m_{A'}^2}, \quad (15)$$

with $\mathcal{C}' \approx 10$. When the typical lifetime ℓ_0 exceeds the length L to the detector, a fraction $\sim L/\ell_0$ decays before the detector, and the number of A' observed is independent of $m_{A'}$:

$$N_{\text{obs}} \sim N_e \mathcal{C}' \epsilon^2 \frac{m_e^2}{m_{A'}^2} \frac{L}{\ell_0} \sim N_e \mathcal{C}' \alpha \epsilon^4 \frac{m_e^2 L}{E_1}. \quad (16)$$

Note that multiple interactions in the target degrade the beam energy significantly and induce A' transverse momenta $\sim 10 \text{ mrad} (\text{GeV}/E_0)^2$ for A' production in the first radiation length. These transverse momenta can be significant for low-energy dumps.

For subsequent discussions, it is useful to translate the signal yields into rates as a function of beam and target parameters. A process X with cross section $\sigma(X)$ occurs with a rate

$$\Phi(X) \sim 0.7 \text{ MHz} \left[\frac{T \cdot I_{\text{beam}}}{\text{nA}} \frac{\sigma(X)}{Z^2 \mu\text{b}} \right], \quad (17)$$

where I_{beam} is the average current, and $T \lesssim 1$ is the target thickness in units of radiation lengths. For example, $m_{A'} = 100 \text{ MeV}$ and $\epsilon = 10^{-4}$ gives $\sigma_{A'} \sim 0.01 Z^2 \text{ pb}$, or a rate of $\Phi_{A'} \approx 0.007 \text{ Hz} \left[\frac{T \cdot I_{\text{beam}}}{\text{nA}} \right]$. In contrast, Bethe-Heitler pair production (Fig. 3) has a total cross section $\sigma_{l^+l^-} \sim Z^2 \mu\text{b}$, or rate $\Phi_{l^+l^-} \approx 0.7 \text{ MHz} \left[\frac{T \cdot I_{\text{beam}}}{\text{nA}} \right]$ for a $\sim 1 \text{ GeV}$ electron beam. Bethe-Heitler pair production is thus a potential background for any A' search, and so our experimental scenarios will be strongly influenced by the need to remove them.

In Appendix C, we discuss the kinematics of Bethe-Heitler production relative to A' production in some detail, and sketch out a set of selection cuts that can be used to suppress the otherwise prohibitively large Bethe-Heitler backgrounds [Fig. 3(b)]. However, a minimal contribution to the background is obtained by replacing the A' by a γ^* [Fig. 3(a)]. To see this, we reinsert the dilepton invariant mass m^2 into the fully differential cross section and consider integrating over a mass window δm , with $\Gamma \ll \delta m \ll m$. The A' and γ^* matrix elements are related by the substitution

$$\frac{\epsilon^2}{m^2 - (m_{A'}^2 + im_{A'}\Gamma)^2} \rightarrow \frac{1}{m^2}. \quad (18)$$

All other terms in the cross section are slowly varying in this window. Treating them as constant, the integration over the mass window bounded by $m \pm \frac{\delta m}{2}$ is straightforward. Substituting (11), we obtain the ratio of fully differential cross sections for A' to γ^* production in this mass window, which is also an upper bound on the total signal to background,

$$\frac{d\sigma(X \rightarrow A'Y \rightarrow l^+l^-Y)}{d\sigma(X \rightarrow \gamma^*Y \rightarrow l^+l^-Y)} = \left(\frac{3\pi\epsilon^2}{2N_f\alpha} \right) \left(\frac{m_{A'}}{\delta m} \right), \quad (19)$$

where N_f is the number of available decay species for the A' , and δm is the width assigned to the γ^* process. Equation (19) summarizes the maximum achievable signal to background ratio that any experiment can achieve in an

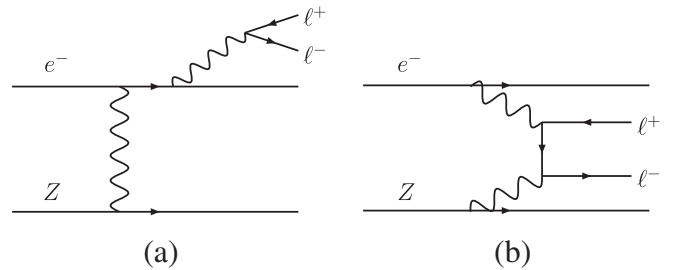


FIG. 3. (a) γ^* and (b) Bethe-Heitler trident reactions that comprise the primary QED background to $A' \rightarrow l^+l^-$ search channels.

$A' \rightarrow \ell^+ \ell^-$ search using only kinematics, with the decay vertex unresolved.

III. BEAM-DUMP CONSTRAINTS AND SENSITIVITY OF CURRENT EXPERIMENTS

In this section, we discuss existing constraints on the ϵ versus $m_{A'}$ parameter space, which are summarized in Fig. 1.

For $m_{A'} > 2m_\mu$, a search for $Y(3S) \rightarrow \gamma A' \rightarrow \gamma \mu^+ \mu^-$ by the *BABAR* collaboration [50] rules out $\epsilon \gtrsim 10^{-3}$ (see also [41]), while the electron and muon anomalous magnetic moments rule out the low-mass-high- ϵ region [51].

Strong constraints are also obtained from electron beam-dump experiments searching for MeV-mass axions. The strongest constraints come from the E137 [52] and E141 [53] experiments at SLAC, and the E774 [54] experiment at Fermilab:

SLAC E137 dumped 30 C of electrons at 20 GeV into aluminum targets [52]. The power of the beam was about 0.2 MW. Beam products traveled through a 200 m hill and an additional 200 m of open region before hitting a (3m)² detector. No candidate events were observed. The contour in Fig. 1 represents an expected signal of 10 events (we have idealized the detector as a circle of radius 1.5 m).

SLAC E141 dumped 2×10^{15} electrons at 9 GeV into a 12 cm tungsten target, with a 10 cm tungsten target used for calibration [53]. The detector was located 35 m from the dump, and the analysis required observing a single decay product carrying over 0.5 times the beam energy with angular acceptance set by a 7.5 cm pipe. Based on the background rates reported by the experiment, the exclusion in Fig. 1 represents an expected signal of 1000 events.

Fermilab E774 dumped 0.52×10^{10} electrons at 275 GeV onto two 28-r.l.-thick (about 19.6 cm) stacks of tungsten plates [54]. The overall target length, including veto counters behind the target, was 30 cm. An electromagnetic calorimeter with an angular acceptance of about 20 cm was placed 7.25 m downstream from the dump. The trigger required an energy deposition of at least 27.5 GeV and no signal from the veto counters. Based on the results reported by the experiment, Fig. 1 represents an expected signal of 17 events.

The approximate formulas given in Sec. II C are sufficient to understand the shape and magnitude of the beam-dump limits shown in Fig. 1: they are bounded above by a diagonal along which many A' may be produced, but all decay within the shielding that stops the beam, and from below by a line of diminishing rate, which is diagonal if the typical decay occurs before the detector position, and approximately horizontal if the average decay length ℓ_0 is larger than the length scale L of the experiment [see Eq. (16)]. Similar limits can be derived for alternative A' decay modes, for example, if the A' decays to dark-sector Higgses with a typical proper lifetime that scales as ϵ^{-4} rather than ϵ^{-2} .

Supernova cooling places a significant constraint on lower ϵ and lighter $m_{A'}$. A proper accounting of supernova limits on the A' is beyond the scope of this paper, but we outline a simple estimate based on scaling similar results for axions [55]. The hot core of a collapsing supernova can cool through production of A' if they decay $\gtrsim 10$ km from the point of production (the mean free path is typically longer than the lifetime). However, neutrino observations of SN1987A confirmed an energy loss over 5–10 seconds of $1\text{--}4 \times 10^{53}$ erg. Following [55], we require the energy loss in A' emission not to exceed 10^{53} erg/s. We take the A' luminosity per unit energy from the core to be

$$\frac{dL}{dE_A} \sim \frac{1}{T_{\text{SN}}} (6 \times 10^{70} \text{ erg/s}) e^2 \epsilon^2 \quad (20)$$

for $E_A < T_{\text{SN}} = 30$ MeV, which is suppressed by T_{SN}/m_p (where m_p is the proton mass) relative to the axion rate [55,56] because the vector emission matrix element is proportional to v^2 , whereas the axion emission matrix element approaches a constant as $v \rightarrow 0$. We impose an additional Boltzmann suppression $e^{-E_A/T}$ for $E_A > T_{\text{SN}}$ and multiply by the fraction $f(E_A) = e^{-10 \text{ km}/\ell_0}$ that leave the supernova core. Requiring that the total luminosity not exceed 10^{53} erg/s, we can exclude the lowermost region in Fig. 1. We emphasize that the luminosity obtained by scaling is only correct within an order of magnitude. An error in the cross section would affect the lower limit in ϵ proportionally, but the upper limit only logarithmically.

Constraints from other experiments are all contained within the limits from the experiments discussed above. For example, the region constrained by the SLAC search for millicharged particles, which also used an electron beam, is contained within E137 [57]. Proton beam dumps can produce A' in radiation directly from the proton or in radiation from electrons produced by the nuclear shower. Both processes produce A' of much lower energy than the primary proton (hard bremsstrahlung off the proton is suppressed by the proton's finite size, and the shower electrons are quite soft). These softer A' typically decay inside the dump. Therefore, proton dumps such as the CHARM experiment at CERN [58] do not exclude new regions, though they do overlap significantly with the E137 exclusion. Likewise, experiments dumping proton beams for other purposes (e.g. neutrino experiments such as MINOS and MINIBOONE) have little or no potential reach beyond E137.

We have also considered potential limits from A' production off cosmic rays impinging on Super-K, AMANDA, and ICE-CUBE detectors, which is dominated by bremsstrahlung off muons near ground level, which must only survive ~ 1 km to reach the detectors. The potential sensitivities of these experiments are contained within the E137 excluded region.

IV. SCENARIOS FOR NEW EXPERIMENTS

The parameter space that new experiments must cover spans a huge range. The A' production cross section and decay width vary as ϵ^2 and thus vary over 10 orders of magnitude. Our purpose in this section is to explore experimental scenarios appropriate to different parameter ranges. For the sake of definiteness, we organize the discussion around parameter points labeled “A” through “E” in Fig. 1. Each choice suggests a different experimental approach, described in the appropriately labeled subsections.

We do not intend here to provide detailed designs; this is the task of those who would actually do the experiments. We do attempt to show that the exploration of this parameter space is experimentally feasible and offer some guidance regarding how to choose design parameters in order to optimize the experimental sensitivity. Because the electron beams at Jefferson Laboratory appear to be an attractive choice for such experiments, we have been guided in our considerations by the beam specifications available there. However, we expect that other attractive options exist elsewhere.

There is a natural dividing line in the parameter space (cf. Fig. 1), corresponding to an A' proper lifetime $c\tau \simeq 80 \mu\text{m}$, comparable to that of the τ lepton. Longer lifetimes allow in principle the determination of a separated decay vertex, while much shorter lifetimes do not. Since determination of the detached vertex is a strong experimental signature, the experimental techniques naturally differ in the two regimes. Beam-dump searches, including our first (and last) scenario, are appropriate to much longer lifetimes. The region near the dividing line has not yet been explored, and microvertex detectors appear quite promising in this range. The second and third scenarios we describe assume this technique.

For very short lifetimes of the A' , the experimental signature is identical to electromagnetic trident production $e + Z \rightarrow 3e$ or $e + Z \rightarrow e + 2\mu$ (where Z is the target), shown in Fig. 3. The simple upper bound discussed in Eq. (19) in Sec. II on the ratio of the A' fully differential cross section to the background trident rate implies that high statistics and resolution are required to have any chance of observing the A' . Fortunately, such a regime does appear to overlap with the capabilities of Jefferson Laboratory spectrometers. Moreover, the upper bound is attained in a sizeable region of the differential phase space where A' production is dominant, if appropriate kinematic cuts are applied on the final-state leptons (see Appendix C). Therefore this parameter region seems in principle to be accessible. Our fourth experimental scenario deals with this case. We will also show that the second and third scenarios we discuss have some interesting new reach in parameter space when used at lower luminosity as high-resolution forward spectrometers.

For the smallest values of ϵ , the primary consideration is simply producing enough A' 's to study experimentally, so beam-dump experiments are the technique of choice. However, it becomes very challenging to design beam dumps with average power exceeding 1 MW. There appears to be a small window of opportunity available for such a search, which would increase the reach beyond that of E137. This comprises the fifth scenario that we discuss.

A. Low power, 10 cm tungsten beam dump; $\epsilon = 10^{-5}$; $m_{A'} = 50 \text{ MeV}$

We consider a 200 MeV primary electron beam incident on a 10 cm tungsten target. Downstream (beyond a thin, but dense, shielding wall, if necessary) is an instrumented decay volume containing a combination of tracking planes, electromagnetic calorimetry, and scintillator triggers. With the chosen values of ϵ and $m_{A'}$, the laboratory decay length of a typical A' of momentum 160 MeV is about 5 cm. The produced A' 's are contained in an angular cone of order 125 mrad. Therefore the tracking system in an experimental region no more than 40 cm (see Fig. 4) downstream of the front of the dump need have transverse dimensions no more than 10 cm to identify the A' decay vertices and measure the angles. Since the decay angles of the electron/positron pair are of order 250 mrad, the calorimeter transverse dimensions can be very modest.

In this scenario, the total yield per incident electron of A' 's containing at least 80% of the beam momentum is about 9×10^{-15} per electron dumped. If the front of the fiducial decay volume can be located immediately behind the 10 cm target, 5% of these A' 's decay outside the target for a rate of 4×10^{-16} per electron dumped. If a thicker shield is necessary to stop soft photons, the yield remains large: 0.1% of the A' decay beyond 30 cm from the front of the dump, for one observable A' decay per 5×10^{16} electrons dumped. In the conservative configuration, with a total of 30 cm of material, a yield of order 30 events would be observed for 0.3 coulombs of electrons dumped (300 nA in an experiment of duration 10^6 seconds). This requires a modest 60 watts of beam power on the tungsten dump.

The length of the fiducial decay region need only be 20 cm to capture the majority of the A' 's emerging from the dump into the decay region. The compact nature of this decay volume suggests the possible use of silicon-strip detectors for the tracking system.

The question of backgrounds must of course be addressed. A fast, dense tracking system seems to be appropriate. With a readout rate at least 10 MHz, and with a continuous incident beam such as exists at Jefferson Laboratory, there would be about 30 000 electrons dumped per readout cycle. The shower products should be absorbed efficiently, and it should be very rare that a prompt calorimeter signal of more than 100 MeV energy deposition occurs, especially because the time resolution of a scintillator trigger/electromagnetic calorimeter system will be

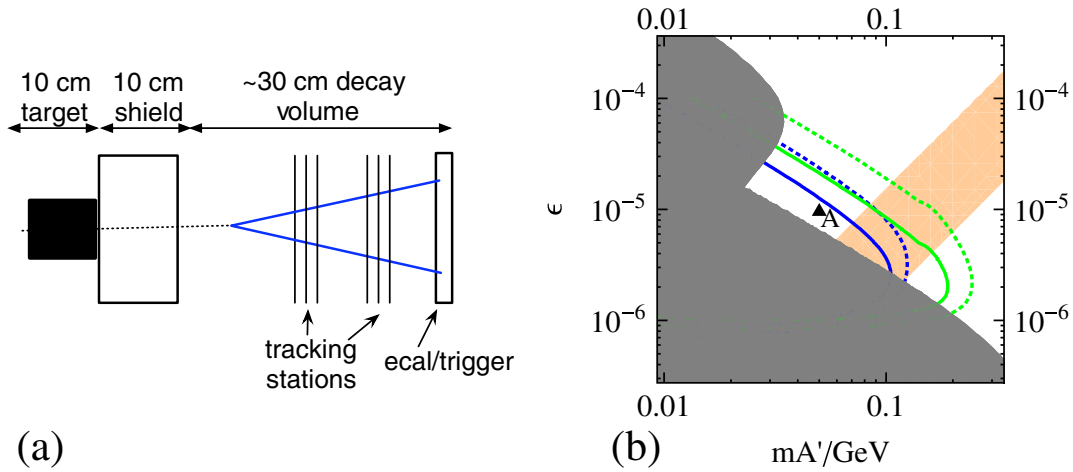


FIG. 4 (color online). (a) Experimental scenario for benchmark point A ($\epsilon \sim 10^{-5}$, $m_{A'} \sim 50$ MeV). An electron beam is incident on a 10 cm thick tungsten target. Behind the target is a 10 cm (or thicker) shield followed by an instrumented decay region consisting of a combination of tracking planes, electromagnetic calorimetry, and scintillator triggers. (b) Reaches of the high- and low-energy dump configurations described in Sec. IV A, delineated by regions with 10 or more events and the following configurations—*Blue (inner) solid contour*: 0.3 C total charge dumped with a 200 MeV electron beam, a 20 cm shield, and a detector with 5 cm radius 50 cm behind the front of the target. The lepton pair must have total energy exceeding 100 MeV. *Blue (inner) dashed contour*: same configuration, but with no shield. *Green (outer) solid contour*: 0.1 C (100 nA beam $\times 10^6$ s) total charge dumped with a 6 GeV electron beam, a 3.9 m shield, and a detector with 10 cm radius 7 m downstream. The lepton pair must have total energy exceeding 3 GeV. *Green (outer) dashed contour*: same configuration, but with 0.9 m of shielding. *Gray contours and orange stripe*: exclusions from past experiments (E137 and E141) and the region that explains DAMA/LIBRA in a simple model—see Fig. 1 for more details.

much better than 100 ns. The residual problems, beyond the scope of this sketch, probably have to do with neutrons and soft photons or x rays.

Evidently, if we lower $m_{A'}$ and increase ϵ in such a way as to decrease neither the rest-frame decay length nor the production rate, the experiment will be easier, since $\gamma c\tau$ is larger and more A' will decay in the detector volume. In Fig. 4, we present our rough estimate of the region of parameter space accessible to the experiment as described.

To extend the reach to larger masses and smaller ϵ , higher beam energies are required. Once the threshold for electroproduction of muons and hadrons has been crossed, the experiment may require a thicker shield, and much higher energies appear advantageous. For example, consider raising $m_{A'}$ and lowering ϵ by a factor of 2, to 100 MeV and 5×10^{-6} . For a beam energy of 6 GeV, the decay length is 2 m. If a 3 m decay volume can be positioned with its upstream end within 4 m of the front of the dump, then a larger fraction of the produced A' 's can be detected than in our original example. This in turn lessens the beam-intensity requirement; an average current of 100 nA, which leads to a dump power of under 1 kW, appears to suffice.

The detector geometry can simply be a longitudinally stretched version of the previous case, with transverse dimensions again quite small, of order 15–20 cm. However, new backgrounds appear. Muons will penetrate the decay volume as well as electromagnetic showers initiated within the hadronic cascade. One leading candidate for background troubles comes from electroproduc-

tion of the ρ , with a leading charged pion from the rho decay undergoing a charge-exchange reaction into a π^0 a few radiation lengths in front of the detector region. We have used the experience obtained in E141 to make rough estimates, which indicate that such backgrounds are surmountable. But the soft backgrounds such as neutrons and hard x rays also need to be carefully studied.

B. Thin-target and double arm spectrometer;

$$\epsilon = 3 \times 10^{-5}; m_{A'} = 200 \text{ MeV}$$

Modern microvertex detectors allow much better lifetime resolution than the above example. When ϵ is increased from the previous example, the rate of A' production per incident electron increases, and a thin target can be used instead of a beam dump. For the parameters of interest here, we consider a 0.1 r.l. tungsten target. We choose a 6 GeV beam with an average current of 100 nA. Downstream of the target is a two-arm minispectrometer with silicon-strip detectors as the tracking elements, backed up with fast calorimeter/scintillator triggers.

With these parameters, the A' production rate (before acceptance) out of the target is about 10 per hour. The angular divergence of the A' beam is only about 5 mrad. The laboratory decay length is about 1 cm, and the decay products of the A' have an average angle of about 35 mrad from the beam axis. A spectrometer with polar angle coverage of 20 to 55 mrad and 50% azimuthal angle coverage has about 25% acceptance for the A' decay products. The trigger requirement includes the demand that the energies in each of the calorimeters are between 1 and 5 GeV,

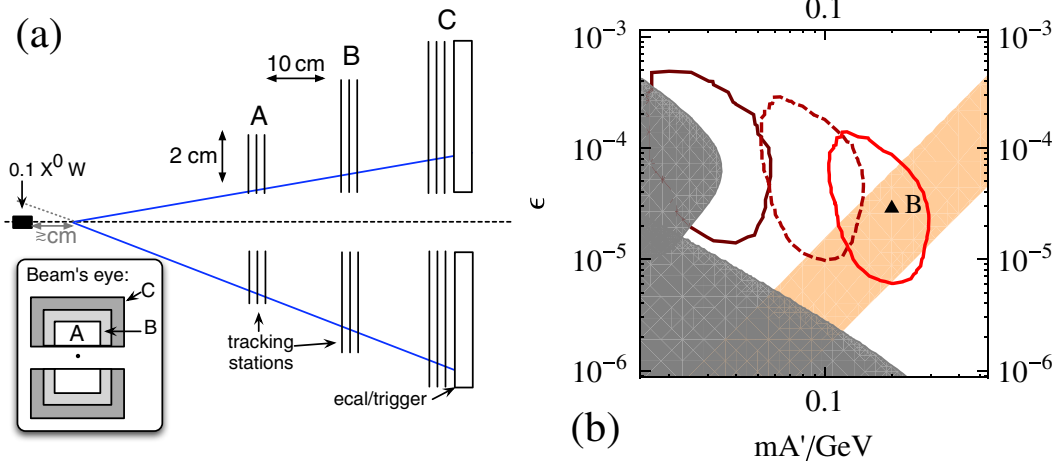


FIG. 5 (color online). (a) Experimental scenario for a small two-arm spectrometer for benchmark point B ($\epsilon \sim 3 \times 10^{-5}$, $m_{A'} \sim 200$ MeV). An electron beam is incident upon a thin 0.1 r.l. tungsten target. A small two-arm spectrometer with silicon-strip trackers and a fast calorimeter or scintillator trigger is downstream from the target. Signal events are identified by requiring a displaced-vertex ~ 1 cm behind the target. More details are given in the text. (b) Regions corresponding to 10 or more events within acceptance in 10^6 sec for three different geometries. *From right to left*: 6 GeV electron beam at 100 nA (0.1 C delivered), with angular acceptance from 20 to 55 mrad and a 1 m long detector (*solid red line*); 6 GeV beam at 5 nA (5×10^{-3} C delivered), with angular acceptance from 10 to 27 mrad in a 2 m-long detector region (*dashed darker red line*); and 2 GeV beam at 0.5 nA (5×10^{-4} C delivered) with the same geometry as the dashed red line (*solid dark red line*). In all cases, we require that the A' carry at least 83% of the beam energy, the track impact parameters at the target exceed $50 \mu\text{m}$, and the reconstructed vertex displacement exceed 1 cm. We assume 50% ϕ coverage. *Gray contours and orange stripe*: exclusions from past experiments (E137 and E141) and the region that explains DAMA/LIBRA in a simple model—see Fig. 1 for more details.

with the sum between 5 and 6 GeV. The tracking system must identify one track in each arm that points to the calorimeter hit (if the calorimeter is segmented) and is consistent with a decay-vertex origin. After reconstruction, additional kinematic constraints provide rejection power. In Fig. 5, we show the reach of this experimental scenario for various geometries and different beam currents.

A major background is simultaneous elastic Coulomb scattering in each arm. An elastically scattered electron deposits 6 GeV in the calorimeter, and is rejected, but the singles rate must be below one per timing window (100 MHz or less for fast calorimeters). This requirement is safely met by the beam intensity quoted above. The elastic-scattering radiative tails will contribute to the trigger, but at a significantly lower rate of 10 kHz or so. Other sources for background triggers, such as Bethe-Heitler pair production (cf. Fig. 3), lead to smaller or comparable trigger rates. When one of the two scattered electrons scatters again in the first layer of silicon, the intersection of the two reconstructed tracks is displaced. We find that the rate for these fake vertices is adequately suppressed if the first layer is placed close to the target, within ~ 5 –10 cm.

Another basic requirement is that the occupancy in the tracking system be acceptably low. High-resolution silicon-strip detectors are beneficial in this regard. Within a cone of opening angle of 10 mrad at a distance of 50 cm downstream of the target, we estimate that the density of electrons and photons produced in the target with energy

above 1 MeV is of order $10^9/\text{cm}^2/\text{s}$. In this scenario, the silicon is placed further from the beam, but this rate serves as a rough upper bound, which would give 1% occupancy for a $1 \text{ cm} \times 25 \mu\text{m}$ strip. While these numbers are encouraging, a serious simulation is certainly required.

C. Silicon-strip layers in a diffuse electron beam; $\epsilon = 10^{-4}$; $m_{A'} = 50$ MeV

At even higher ϵ and lower masses, there exists the option of halving the number of silicon-strip tracking elements and placing them directly into a defocused primary electron beam of low intensity. For this study, we choose the beam size to be about $1 \text{ cm} \times 1 \text{ cm}$ and the beam energy to be 1 GeV. The beam intensity is limited by silicon occupancy to about $10^8 \text{ e}^-/\text{s}$, if we require occupancy of about 1% in $1 \text{ cm} \times 25 \mu\text{m}$ strips with a timing window of 20–50 ns.

Triggering is again accomplished by a calorimeter, with a strategy similar to case B and the same limitations. For A' masses of 20–50 MeV, decay opening angles ~ 20 –50 mrad are anticipated, so the calorimeter must extend close to the beam. For simplicity we consider an annular calorimeter with angular coverage above 20 mrad (for example, located at 2.5 meters from the target, with inner radius of 5 cm). The beam electrons emerge from a 0.1 radiation-length tungsten target in a Molière distribution, with typical transverse momenta of 5 MeV. Therefore less than 1% of the electron beam hits the calorimeter,

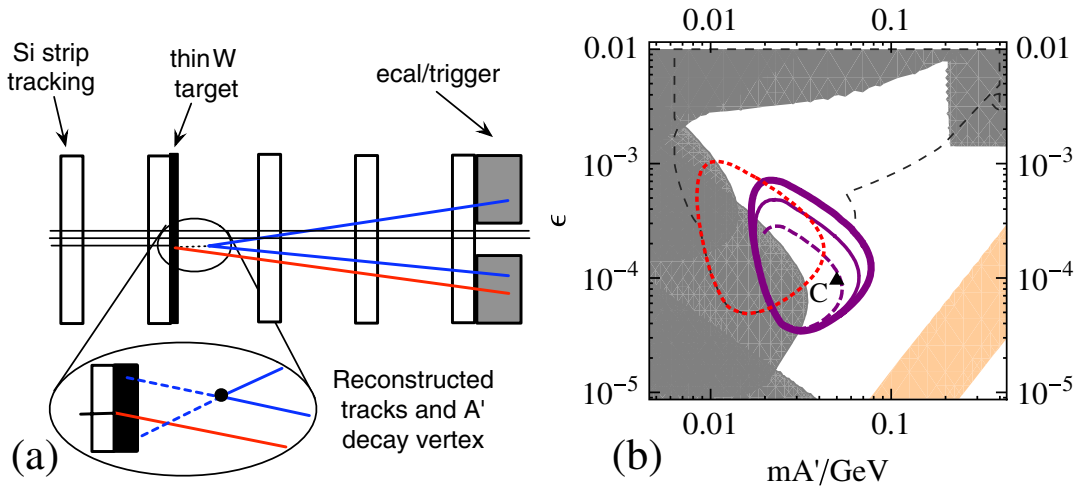


FIG. 6 (color online). (a) Experimental scenario for benchmark point C ($\epsilon \sim 10^{-4}$, $m_{A'} \sim 50$ MeV). Silicon-strip tracking elements, together with a 0.1 r.l. (300 μm) tungsten target directly behind one of the elements, are inserted into a 1 GeV diffuse (1 cm \times 1 cm) electron beam of intensity $\leq 10^8$ e^-/s . Triggering is accomplished by an annular calorimeter with angular coverage above 20 mrad (e.g. 2 cm inner radius, 1 m downstream) by demanding three coincident hits carrying the beam energy. Signal events give rise to measurable impact parameters for the leading two tracks, and the excellent tracking provided by this design exploits this feature to reject background. Invariant-mass reconstruction can provide an additional search variable (see Sec. IV D). More details are given in the text. (b) *Concentric solid and dashed purple contours*: Regions with detectable signal yield ≥ 10 events, background rejection of $\sim 10^{-6}$ (yielding $S/B \geq 1$), and an impact parameter of at least 33 μm , 66 μm , or 150 μm , respectively, for the contours from the outside in. We assume a run time of 10^6 s at 10^8 e^-/s . *Red dotted contour*: Analogous sensitivity with lower average current (10^7 e^-/s) and a smaller calorimeter aperture (10 mrad). *Thin black dashed line*: a rough estimate of the total region of sensitivity that could be accessible to this geometry using both displaced-vertex discrimination and invariant-mass search windows with good momentum resolution (see Sec. IV D). *Gray contours and orange stripe*: exclusions from past experiments [E137, E141, E774, electron and muon anomalous magnetic moments, and $Y(3S)$ resonance searches] and the region that explains DAMA/LIBRA in a simple model—see Fig. 1 for more details.

leading to a $\lesssim 1$ MHz singles rate, which is high but manageable for a trigger requiring two hits.

With these parameters the A' production rate is about 1 every ten hours. Off-line track reconstruction can be used to remove the backgrounds associated with the Coulomb scattering pileup and other background sources, in particular, Bethe-Heitler pair production from the target. The quality of the experiment will depend crucially on the precision of the vertex reconstruction using the silicon-strip information. Our sample point has typical impact parameter ~ 160 μm and laboratory decay lengths of order 2.3 mm, which should be cleanly resolvable. The sensitivity of this configuration, assuming several different resolutions, is illustrated in Fig. 6.

For smaller masses, the calorimeter must be placed at a narrower angle or the beam energy reduced. In either case, the Molière scattering becomes more acute. On the tails of the Molière distribution, one can compensate by lowering the intensity of the beam. At low beam intensities, a fast scintillator/calorimeter trigger system will resolve the passage of individual electrons in the beam (in a continuous wave machine like CEBAF). Therefore, if the scintillator/calorimeter system is segmented (e.g. scintillating fiber calorimetry), the trigger requirement can be simultaneous deposition of the beam energy in more than one detection element—typically three. For larger masses, the beam

intensity would have to be increased, and the silicon-strip occupancy presents a sharp barrier.

D. High-resolution, high-rate trident spectrometer; $\epsilon = 3 \times 10^{-4}$; $m_{A'} = 1$ GeV

Large A' masses present two challenges: a low production rate and short A' lifetime. In the absence of a displaced vertex, the A' can only be observed as a small peak on the electromagnetic trident background. Reducing these backgrounds as much as possible is essential here. Additionally, targets with somewhat lower Z than tungsten are preferable in this high A' mass range in order to maintain charge coherence in scattering. For definiteness, we shall discuss the di-muon final state, though it is arguable that the electron-positron final state is preferable.

As discussed in Sec. II, the trident background arises from two subprocesses, which we call radiative and Bethe-Heitler (c.f. Fig. 3). The radiative process gives an upper bound on the ratio of signal to background as in Eq. (19). The Bethe-Heitler process has a much larger ($\sim 100 \times$) cross section than the radiative trident process due to collinear logarithmic enhancements in the $e \rightarrow e\gamma$ splitting and subprocess $\gamma\gamma \rightarrow \mu\mu$. These enhancements can be avoided by demanding kinematically symmetric $\mu\mu$ decay products carrying the majority of the beam energy, and by

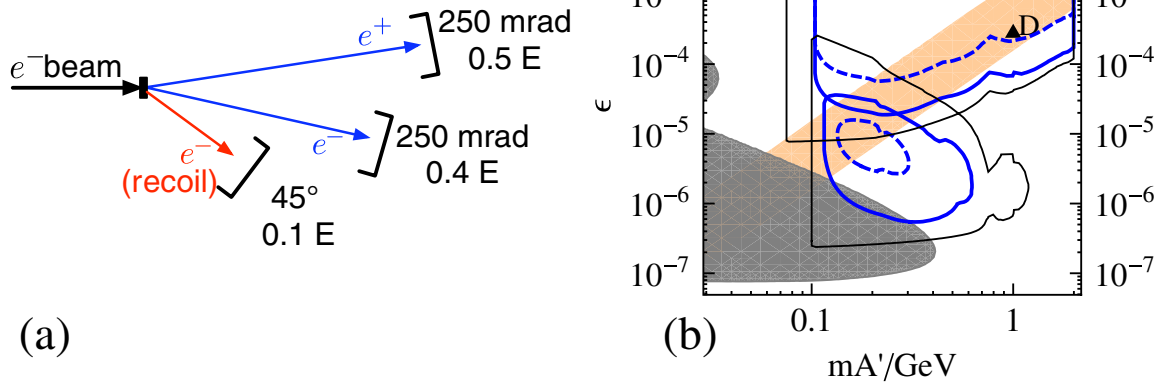


FIG. 7 (color online). (a) Schematic diagram of an experimental scenario for benchmark point D ($\epsilon \sim 3 \times 10^{-4}$, $m_{A'} \sim 1$ GeV). An electron beam with an energy of ~ 6 GeV and a current of about $100 \mu\text{A}$ – $200 \mu\text{A}$ is incident upon a 0.1 r.l. aluminum target for 10^6 seconds. A wide-angle high-resolution spectrometer allows triggering on events in which one electron and one positron carry most of the beam energy. The signal is distinguished from background events with the help of various kinematic selection cuts (relatively symmetric $\ell^+\ell^-$ final state and possible recoil electron tagging) and a “bump hunt”—see text and Appendix C for further details. (b) Various estimates of the possible reaches of a wide-angle spectrometer for the parameters above, with (bottom) and without (top) tagging vertices displaced by >1 cm to reject background. In each case, the outer thin black line represents a significant total rate, with no geometric acceptance requirements [$S/\sqrt{B} > 5$ in the no-vertex (top) region, 10 or more events in the vertex (bottom) region]. The thick blue curve shows the reach when decays are required to land more than 200 mrad away from the beam line, and the inner dotted curves assume an additional 1% signal efficiency from acceptance. In these two cases, each curve represents the total reach obtained by running at several beam energies. *Gray contours and orange stripe*: exclusions from past experiments [E137, E141, E774, electron and muon anomalous magnetic moments, and $Y(3S)$ resonance searches] and the region that explains DAMA/LIBRA in a simple model—see Fig. 1 for more details.

demanding that the recoiling electron (if it can be identified) scatter at a wide angle. This preserves the large logarithm in the forward-peaked A' production cross section, while regulating all logs in the Bethe-Heitler process. These selections are discussed further in Appendix C.

In addition to the trident processes, radiation of real photons by incident electrons, and their subsequent conversion in the target, must be considered. This process is naively enhanced by $\mathcal{O}(T/\alpha)$ relative to Bethe-Heitler trident production, but can be rejected effectively with the same kinematic cuts. It is, of course, reducible by thinning the target, which allows a compensating increase in average beam current. We have not considered pile-up processes, but assume they are small when the three products are required to reproduce the beam energy within resolution.

For this scenario, we consider a 0.1 r.l. aluminum target in a 4 GeV beam. The total yield of A' 's is roughly 10^{-16} per incident electron. If we assume an average beam current of $250 \mu\text{A}$ (beam power of 1 MW) and an experimental duration of 10^6 sec, the total rate of A' production is of order one per second, or $\geq 10^5$ per experiment. These are emitted in a cone of size ~ 100 mrad, with decay products at opening angles near 250 mrad and the recoiling electron at a rather wide angle, 0.5 radians. The yield of background tridents having a di-muon

mass within 1% of the A' mass is, according to (19), about 300 times larger, or 3×10^7 per experiment. The estimated cumulative sensitivity of this configuration, and similar ones obtained by lowering the beam energy down to ~ 1 GeV, is illustrated in Fig. 7. To obtain the contours in this figure, we require that $S/\sqrt{B} \geq 5$, i.e. $(S/\epsilon_b B_0) \times S \geq 25$, where S is the signal rate, and B is the background rate, B_0 , times the background rejection efficiency ϵ_b . We use Eq. (19) to obtain S/B_0 , and choose reasonable values for ϵ_b .

The signal rate above is, indeed, larger than necessary for the A' resonance to be statistically significant. A less ambitious (and perhaps more realistic) experiment would also suffice for discovery. There are at least three ways to back off from this scenario. One way is evidently to improve the mass resolution. A second way is to reduce the beam intensity, keeping the acceptance complete. A reduction in beam current by a factor of 100 would still leave a viable signal. The third way is to reduce the acceptance; a 1% acceptance by itself would again leave a viable signal.

Optimization involves a choice of a combination of these factors. Jefferson Laboratory looks like an especially appropriate venue for this scenario, with two spectrometers with very good electron momentum resolution. In particular, the small-acceptance, high-rate spectrometers in Hall

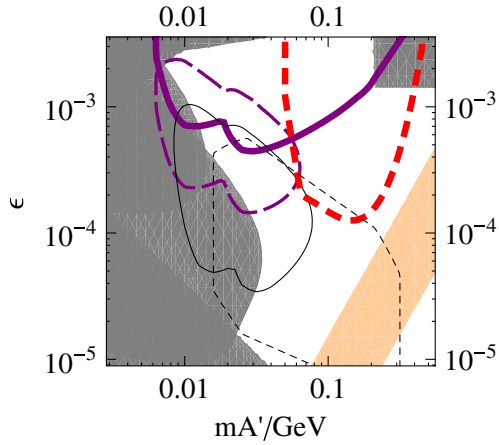


FIG. 8 (color online). Estimated reach for the geometries of scenarios B (thick dashed red line) and C (thick solid and long-dashed purple lines) in “bump-hunt” operation with upgraded mass resolution. For reference, the approximate expected reach of clean vertex-based searches discussed in Secs. IV B and IV C is given by the thin black dashed contour and the thin black solid contour, respectively. *Thick dashed red contour*: The combined reach (with $S/\sqrt{B} \geq 5$) of the two two-arm spectrometer geometries introduced in Sec. IV B and Fig. 5 with a 6 GeV beam. *Thick solid purple Contour*: $S/\sqrt{B} \geq 5$ for the combined reach of the different “diffuse-beam” scenarios in Sec. IV C, assuming 1% mass resolution. *Long-dashed purple Contour*: Same as the thick solid purple contour, but using vertexing to reduce backgrounds, with an assumed “optimistic” rejection of 10^{-2} for an impact parameter cut of $10 \mu\text{m}$ applied to the lepton pair. *Grey contours and orange stripe*: exclusions from past experiments [E137, E141, E774, electron and muon anomalous magnetic moments, and $Y(3S)$ resonance searches] and the region that explains DAMA/LIBRA in a simple model—see Fig. 1 for more details.

A has momentum resolution of order 10^{-4} and the large-acceptance Hall B CLAS detector has electron momentum resolution better than 1% [59]. Therefore it would seem that using an electron-positron pair for the A' decay products may make more sense than using a di-muon pair. However, we feel further investigation is best done with the aid of expertise within the Jefferson Laboratory experimental community.

1. High-resolution forward spectrometers at lower luminosity

As we lower $m_{A'}$ while keeping ϵ large, the production angles may become too low for big spectrometers such as those found in Hall A at JLab. The geometries of the detectors sketched in Secs. IV B and IV C may be more appropriate. The growth of the production cross section as $1/m_{A'}^2$ compensates for the lower average currents demanded by these scenarios (10–100 nA for the two-arm spectrometer B [described in Sec. IV B] and $10^8 \text{ e}^-/\text{s}$ when tracking planes are inserted in the beam as in C [described in Sec. IV C]).

In scenarios B and C, in the interest of simplicity, we did not assume a high-mass resolution for the spectrometers. However, a high-mass resolution, e.g. via addition of magnetic fields, is not at all impractical in principle. Assuming a 1% mass resolution, the potential sensitivity of these modified scenarios is sketched in Fig. 8. Again, it will be important to detect the wider-angle recoil electron in order to reduce backgrounds. This requires increasing the tracking and calorimeter coverage to around 250 mrad for the two-arm spectrometer B as well as for the diffuse-beam, collinear configuration C.

The gap between the spectrometer and resolved vertex regimes coincides with A' decay lengths of order the 1σ vertex resolution of a given detector. In this regime, one can gain sensitivity by imposing a loose impact parameter/vertex requirement that reduces background rates by a few orders of magnitude. Clearly, this strategy is plagued by the difficulties of both the spectrometry and vertexing approaches, and would only be attempted in a later stage when the detector and backgrounds are well understood. We do not discuss it further.

E. High power, low-energy beam-dump; $\epsilon = 5 \times 10^{-8}$; $m_{A'} = 50 \text{ MeV}$

Values of ϵ below the E137 limit require very intense beams simply to produce enough A' 's to detect. Beam power limitations force one downward in beam energy. We choose a 200 MeV beam of electrons with an average current of 5 mA, representing a beam power of 1 MW (for reference, the beam power of E137 was about 0.2 MW). The A' production rate is about 2×10^{-19} per electron dumped. The laboratory decay length is about 2.5 km. The divergence of the A' beam is about 100 mrad. We consider a decay region 5 m long, with its front end located 5 meters downstream of the dump. A tracking system, perhaps in the style of E137, with transverse dimensions $2 \text{ m} \times 2 \text{ m}$ is distributed throughout the decay volume to capture the decay products from the A' decays. It is surrounded by electromagnetic calorimetry designed to efficiently capture the electrons and positrons emergent from the tracking volume (see Fig. 9). With these parameters, the yield of detected A' 's is marginal—about 5–10 per 10^6 seconds.

This scenario has not been optimized, and other versions less awkward can be contemplated. However, the region of the exclusion plot that is covered by any such experiment will be modest. Therefore a real design is likely to be opportunistic. If the experiment can be run parasitically for a long period of time, the benefit-to-cost ratio may rise sufficiently high to make such an effort attractive.

If one contemplates utilizing a higher-energy dump of 1 MW power, then the number of electrons dumped decreases, and keeping $m_{A'}$ and ϵ fixed, the yield of A' 's decreases as well. The region of sensitivity at A' masses of

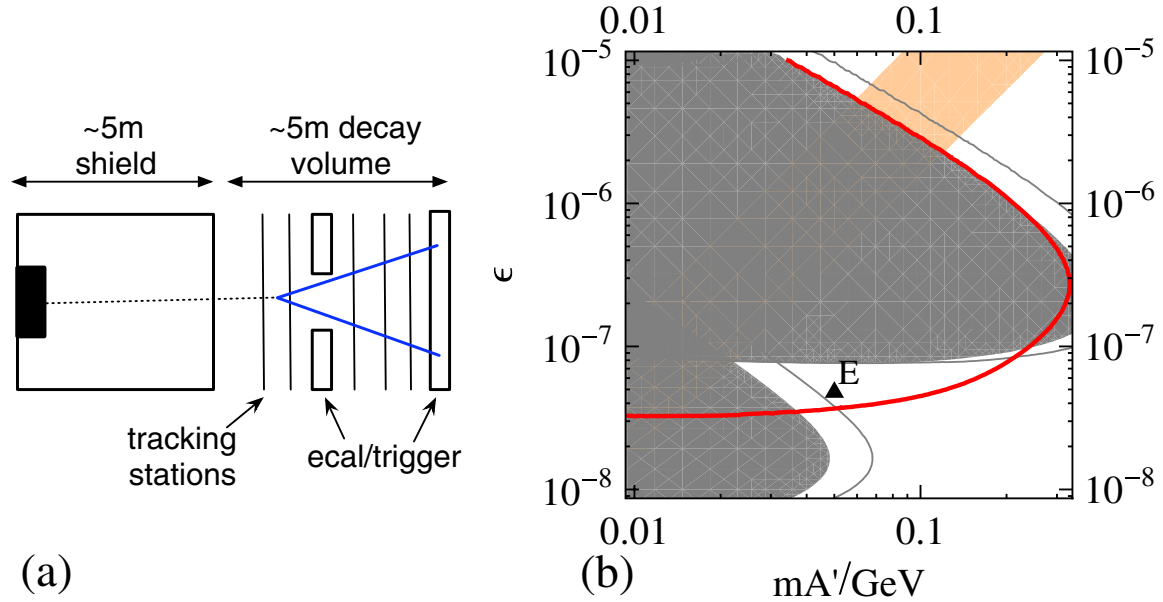


FIG. 9 (color online). (a) Schematic diagram of a beam-dump design for benchmark point E ($\epsilon \sim 5 \times 10^{-8}$, $m_{A'} \sim 50$ MeV). A 200 MeV electron beam with a large current of about 5 mA (delivering 1 MW in power) is incident upon a thick tungsten target that together with shielding is about 5 m in length. Behind the shielding is a decay region 5 m long, consisting of a tracking system ($2 \text{ m} \times 2 \text{ m}$ transverse to the beam line) and surrounded by electromagnetic calorimeters—see text for further details. (b) *Solid red contour*: 10 events with A' energies above 100 MeV after the experiment has run for 10^6 s (5000 C total charge dumped). *Gray contours and orange stripe*: exclusions from past experiments (E137 and SN1987A) and the region that explains DAMA/LIBRA in a simple model—see Fig. 1 for more details.

about 200 MeV should, to a fair approximation, merge with the reach of E137, as estimated in Fig. 9.

V. DISCUSSION AND CONCLUSIONS

In this paper, we have described five scenarios for fixed-target experiments that probe kinetically mixed $U(1)$'s with MeV–GeV masses. Kinetic mixing of size $\epsilon \sim 10^{-2}$ – 10^{-8} between a light gauge boson and the photon can be generated by loops of particles at any mass scale, with the magnitude determined by the structure of high-scale physics. An MeV–GeV mass for the A' can in turn be generated from the weak scale, especially in a supersymmetric context. An A' in this mass range is also of interest as a possible explanation of several current dark matter anomalies.

The parameter space of A' mass $m_{A'}$ and mixing ϵ has been constrained from two corners by existing data. Beam-dump experiments and supernovas exclude the low-mass, small- ϵ region. Larger $\epsilon \sim 10^{-3}$ – 10^{-2} are constrained for a broad range of masses by lepton anomalous magnetic moments and B -factory searches.

The five approaches we have described cover the remaining parameter space using fixed-target experiments of various geometries and 200 MeV – 6 GeV beams. A natural extension of past beam dumps, with modest intensity and 10 cm – 1 m length, can fill in the crevice of parameter space between past beam dumps. Beam dumps are not well suited to searching for A' with less displaced decays.

For these parameter ranges, thin-target experiments are required.

Any thin-target experiment must contend with the backgrounds from electromagnetic electron scattering and trident production, which can be tackled with a combination of kinematics and displaced-vertex selection. Depending on $m_{A'}$, more forward or wide-angle geometries are called for, and small-scale silicon microstrip tracking can be utilized to isolate displaced decays. We have considered three such scenarios: a forward two-arm spectrometer, a collinear detector in a diffuse, low-intensity beam, and a wide-angle spectrometer. Together, they are sensitive in the range $\epsilon \sim 10^{-5}$ – 10^{-3} for A' masses from 10 MeV to 1 GeV.

The wide-angle scenario is of particular interest, because existing spectrometers can cover a large fraction of its reach. The Hall A spectrometers and the CLAS detector [59] at JLab seem well suited for initial searches, and other labs may have comparable capabilities.

Searches at low ϵ , below the reach of the dump experiment E137, are limited by practical rate limitations. Power above a megawatt (MW) is difficult to sustain, making $\epsilon \sim 10^{-8}$ – 10^{-7} inaccessible with beams of any energy in under a year of running. Our fifth scenario saturates this limit, with a 200 MeV MW dump, which can possibly be accommodated at the JLab Free-Electron Laser accelerator.

When combined with existing limits, these five scenarios can either confirm the existence of new $U(1)$ gauge forces at low masses or close the door on their most likely parameter range.

For masses below the electron threshold, very different experimental techniques are called for. These have been developed in [60–68].

We have restricted our discussion to the simplest scenario: a single $U(1)$ gauge boson that decays directly to electrons. In a larger “dark sector”, somewhere between this minimal scenario and the full complexity of standard model physics, decays within the dark sector dominate [41]. These dark-sector cascades can return some or all of the A' energy to standard model-charged particles, with lifetimes controlled by ϵ^{-2} for vector bosons and much longer lifetimes $\propto \epsilon^{-4}$ for scalars. The limits and reaches discussed here apply directly to any spin-1 bosons in the dark sector that decay directly to a lepton pair. These experiments are also sensitive to dark-sector cascades involving spin-0 states, with appropriately deformed exclusion regions not discussed here. Besides frameworks with kinetically mixed $U(1)$, these experiments are sensitive to direct production of light (pseudo)scalars (e.g. [69–73]). It is likely that related designs more optimally cover these scenarios.

We have focused here on experimental approaches tailored to A' searches in electron beams, but analyses in this spirit may be possible with existing data, for example, by using beam-halo impacts in collider experiments or neutrino production beams and detectors such as those at Fermilab and KEK. We also have not explored the potential of muon-beam experiments, which may be ideal for searches for A' 's above the muon mass, which are produced with rates comparable to those for an electron beam, but with much lower electromagnetic backgrounds.

ACKNOWLEDGMENTS

We thank Andrei Afanasev, Dan Dale, Alex Dzierba, and Richard Jones for information regarding opportunities at JLab for implementing this program. We are grateful to Mathew Graham, John Jaros, Aaron Roodman, and Jay Wacker for feedback and discussion regarding our experimental scenarios, and to Savas Dimopoulos, Michael Peskin, Matt Reece, Jesse Thaler, and Lian-Tao Wang for many fruitful discussions. We especially thank Takashi Maruyama for providing us with background estimates for the forward two-arm spectrometer design and for providing calculations of downstream particle densities using FLUKA. R. E. and P. S. are supported by the U.S. DOE under Contract No. DE-AC02-76SF00515.

APPENDIX A: A' PRODUCTION FORMULAS

In this appendix, we first present the cross section for the production of the massive $U(1)'$ “dark photon,” A' , by initial- or final-state radiation off a single electron hitting a fixed target of atomic number Z . This process is analogous to photon bremsstrahlung, except that the coupling of the A' to electrons is $\epsilon \cdot e$ and the A' mass, $m_{A'}$, is much

larger than the electron mass, m_e , which significantly alters both the kinematics and the rate of the process. The qualitative behavior has already been summarized in Sec. II.

We want to calculate the A' production cross section

$$\frac{d\sigma(e(p) + Z(P_i) \rightarrow e(p') + A'(k) + Z(P_f))}{dE_{A'} d\cos\theta_{A'}} \quad (\text{A1})$$

in the Weizsäcker-Williams approximation following [46–48], where $k = (E_{A'}, \vec{k})$ is the momentum of the outgoing A' , $\theta_{A'}$ is the angle of its momentum relative to the incoming electron momentum \vec{p} in the lab frame, $p = (E_0, \vec{p})$ and $P_i = (M_i, \vec{0})$ are the initial momenta of the electron and the target of mass M_i and atomic number Z , and $p' = (E', \vec{p}')$ and P_f are the outgoing four-momenta of the electron and target, which are integrated over.

In the frame of the incoming electron, the rapidly moving atom sources a cloud of effective photons, off which the electron scatters to radiate an A' . Though these photons are spacelike, their virtuality is small compared to other invariants in the problem (for example, $m_{A'}^2$), so that the interaction of the electron with the target is dominated by transverse polarizations. Therefore, it is related to the cross section for real-photon scattering, $e(p)\gamma(q) \rightarrow e(p')A'(k)$ with $q = P_i - P_f$ by [48]

$$\frac{d\sigma(p + P_i \rightarrow p' + k + P_f)}{dE_{A'} d\cos\theta_{A'}} = \left(\frac{\alpha\chi}{\pi} \right) \left(\frac{E_0 x \beta_{A'}}{(1-x)} \right) \frac{d\sigma(p + q \rightarrow p' + k)}{d(p \cdot k)} \Bigg|_{t=t_{\min}}, \quad (\text{A2})$$

where

$$x \equiv E_{A'}/E_0, \quad t \equiv -q^2. \quad (\text{A3})$$

We specify the kinematics at $t = t_{\min}$ and the effective photon flux $\frac{\alpha\chi}{\pi}$ below. Note that t is not one of the Mandelstam variables for the $2 \rightarrow 2$ process, which will be denoted by t_2 —see below.

For a given A' four-momentum k , the virtuality t has its minimum value t_{\min} when \vec{q} is collinear with the three-vector $\vec{k} - \vec{p}$. Solving the mass-shell conditions $p'^2 = (q + p - k)^2 = m_e^2$ and $P_f^2 = (P_i - q)^2 = M_i^2$ with the collinear geometry, and keeping only leading effects in

$$\frac{m_{A'}^2}{E_k^2}, \quad \frac{m_e^2}{E'^2}, \quad \theta_{A'}, \quad \frac{|\vec{q}|}{E'} \quad (\text{A4})$$

(with $|\vec{q}|$ defined below), we find

$$q^0 = |\vec{q}|^2/2M_i \approx 0, \quad |\vec{q}| = \frac{U}{2E_0(1-x)}, \quad (\text{A5})$$

$$t_{\min} = -q_{\min}^2 \approx \left(\frac{U}{2E_0(1-x)} \right)^2, \quad (\text{A6})$$

where

$$U \equiv U(x, \theta_{A'}) = E_0^2 \theta_{A'}^2 x + m_{A'}^2 \frac{1-x}{x} + m_e^2 x. \quad (\text{A7})$$

At this kinematics,

$$-\tilde{u} \equiv m_e^2 - u_2 = 2p \cdot k - m_{A'}^2 = U, \quad (\text{A8})$$

$$\tilde{s} \equiv s_2 - m_e^2 = 2p' \cdot k + m_{A'}^2 = \frac{U}{1-x}, \quad (\text{A9})$$

$$t_2 = (p - p')^2 = -\frac{Ux}{1-x} + m_{A'}^2, \quad (\text{A10})$$

where s_2 , t_2 , and u_2 are the Mandelstam variables for the $2 \rightarrow 2$ process. The cross section for the $2 \rightarrow 2$ process is therefore

$$\begin{aligned} \frac{d\sigma}{d(p \cdot k)} &= 2 \frac{d\sigma}{dt_2} \approx \frac{1}{8\pi(s_2 - m_e^2)^2} |\mathcal{M}|^2 \\ &= \frac{4\pi\alpha^2 \epsilon^2}{\tilde{s}^2} \left(\frac{\tilde{s}}{-\tilde{u}} + \frac{-\tilde{u}}{\tilde{s}} + \frac{2m_{A'}^2 t_2}{-\tilde{u} \tilde{s}} \right) \\ &= (4\pi\alpha^2 \epsilon^2) \frac{(1-x)}{U^2} \left[1 + (1-x)^2 \right. \\ &\quad \left. + \frac{2(1-x)^2 m_{A'}^2}{U^2} \left(m_{A'}^2 - \frac{Ux}{1-x} \right) \right], \quad (\text{A11}) \end{aligned}$$

where we have dropped the t dependence of $\frac{d\sigma}{dt_2}$ and terms of order m_e^2 in $|\mathcal{M}|^2$. Therefore, the Weizsäcker-Williams approximation to the cross section (A1) is given by

$$\begin{aligned} \frac{1}{E_0^2 x} \frac{d\sigma_{3 \rightarrow 2}}{dx d\cos\theta_{A'}} &= (8\alpha^3 \epsilon^2 \chi \beta_{A'}) \left[\frac{1-x + \frac{x^2}{2}}{U^2} \right. \\ &\quad \left. + \frac{(1-x)^2 m_{A'}^2}{U^4} \left(m_{A'}^2 - \frac{Ux}{1-x} \right) \right], \quad (\text{A12}) \end{aligned}$$

where $\beta_{A'} \equiv \sqrt{1 - m_{A'}^2/E_0^2}$. The x -differential cross section is obtained by integrating (A12) with respect to $\theta_{A'}$ (we will see below that χ actually depends on $\theta_{A'}$, but this can be neglected to excellent approximation). The first term in square brackets integrates to

$$\frac{1-x + \frac{x^2}{2}}{U(x, \theta_{A'} = 0)}. \quad (\text{A13})$$

In the limit $m_{A'} \rightarrow 0$, this becomes the standard photon bremsstrahlung result with a $\frac{1}{x}$ singularity, while the second term in the square brackets vanishes. However, finite $m_{A'}$ regulates this singularity, and in the case of interest, namely, $m_{A'} \gg m_e$, we have $U(x, 0) \approx m_{A'}^2 \frac{1-x}{x}$. The second term integrates to $-\frac{x^2}{6U(x, 0)} + \mathcal{O}(m_e^2 U^2)$, so that

$$\begin{aligned} \frac{d\sigma_{3 \rightarrow 2}}{dx} &= (8\alpha^3 \epsilon^2 \chi \beta_{A'}) \left(m_{A'}^2 \frac{1-x}{x} + m_e^2 x \right)^{-1} \\ &\quad \times \left(1 - x + \frac{x^2}{3} \right). \quad (\text{A14}) \end{aligned}$$

This has an approximate soft electron singularity, regulated by the electron mass at $(1-x)_{c1} = m_e^2/m_{A'}^2$. Though not explicit in this formula, our approximations also break down if the electron energy $(1-x)E_0 \lesssim |\vec{q}|$; this also regulates the cross section, cutting off $\log(1-x)$ at $(1-x)_{c2} = m_{A'}^2/E_0^2$. Since one cutoff or the other is always larger than its geometric mean m_e/E_0 , the A' is always produced from a relativistic electron. The x -integrated cross section is therefore

$$\sigma \approx \frac{8}{3} \frac{\alpha^3 \epsilon^2 \beta_{A'}}{m_{A'}^2} \chi \log\left(\frac{1}{(1-x)_c}\right), \quad (\text{A15})$$

$$(1-x)_c = \max\left(\frac{m_e^2}{m_{A'}^2}, \frac{m_{A'}^2}{E_0^2}\right). \quad (\text{A16})$$

As we have noted in Sec. II, the characteristic angle of A' emission is set by $U(x, \theta_{A'}) - U(x, 0) \sim U(x, 0)$, so $\theta_{A'} \sim \frac{m_{A'} \sqrt{1-x}}{E_0}$, where the median value of $1-x$ is $\overline{1-x} \sim \max\left(\frac{m_e}{m_{A'}}, \frac{m_{A'}}{E_0}\right)$. This is parametrically smaller than the angle of the A' decay products with respect to the incoming electron, namely, $\sim m_{A'}/E_0$.

We turn next to the definition of χ , which is an effective flux of photons integrated from $t = t_{\min}$ to t_{\max} , the total center-of-mass energy of the collision. We refer the reader to [46,47] for more details.

For a general electric form factor $G_2(t)$,

$$\chi \equiv \int_{t_{\min}}^{t_{\max}} dt \frac{t - t_{\min}}{t^2} G_2(t). \quad (\text{A17})$$

[We note that the other form factor, $G_1(t)$, contributes only a negligible amount in all cases of interest.] Although the virtual photon propagator squared, $1/t^2$, is dominated at $t = t_{\min}$, the final-state phase space is proportional to $dt(t - t_{\min})$, so that virtual photons at all scales contribute to A' production. As discussed in [46,47], the physical upper bound may be set not by the center-of-mass energy, but by $t_{\max} \sim m_{A'}^2$, at which the full $2 \rightarrow 3$ matrix element begins to shut off.

For most energies in question, $G_2(t)$ is dominated by an elastic component

$$G_{2,\text{el}}(t) = \left(\frac{a^2 t}{1 + a^2 t} \right)^2 \left(\frac{1}{1 + t/d} \right)^2 Z^2, \quad (\text{A18})$$

where the first term parametrizes electron screening (the elastic atomic form factor) with $a = 111Z^{-1/3}/m_e$, and the second finite nuclear size (the elastic nuclear form factor) with $d = 0.164 \text{ GeV}^2 A^{-2/3}$. We have multiplied together the simple parametrizations used for each in [46]. The

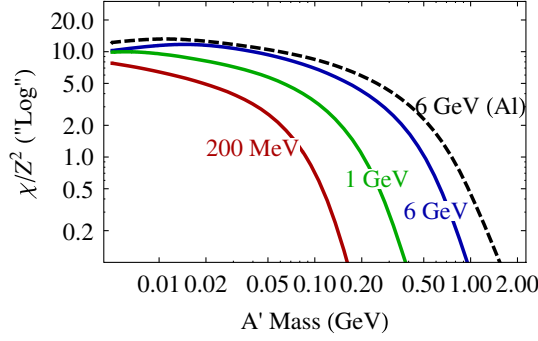


FIG. 10 (color online). The factor $\mathcal{L}og = \chi/Z^2$ appearing in Eqs. (5) and (8) in Sec. II. Solid lines from left to right correspond to beams of energy 200 MeV, 1 GeV, and 6 GeV, respectively, incident on a tungsten target. The dashed line corresponds to a 6 GeV beam incident on an aluminum target.

logarithm from integrating (A17) is large for $t_{\min} < d$, which is true for most of the range of interest. However, for heavy A' , the elastic contribution is suppressed and is comparable to an inelastic term,

$$G_{2,\text{in}}(t) = \left(\frac{a'^2 t}{1 + a'^2 t} \right)^2 \left(\frac{1 + \frac{t}{4m_p^2} (\mu_p^2 - 1)}{(1 + \frac{t}{0.71 \text{ GeV}^2})^4} \right)^2 Z, \quad (\text{A19})$$

where the first term parametrizes the inelastic atomic form factor and the second the inelastic nuclear form factor, and where $a' = 773Z^{-2/3}/m_e$, m_p is the proton mass, and $\mu_p = 2.79$ [46]. This expression is valid when $t/4m_p^2$ is small, which is the case for $m_{A'}$ in the range of interest in this paper. One can show that the contribution from the other inelastic nuclear form factor $G_1(t)$ is negligible.

At high masses, these simple parametrizations of the form factors are uncertain at the order-of-magnitude level. Using $G_{2,\text{el}} + G_{2,\text{in}}$ in (A17), and setting $t_{\min} = (m_{A'}^2/2E_0)^2$, $t_{\max} = m_{A'}^2$, we obtain χ/Z^2 shown in Fig. 10.

APPENDIX B: PRODUCTION FROM THIN AND THICK TARGETS OF A' 'S WITH FINITE LIFETIME

Consider an electron beam with energy E_0 incident on a target. The total number of A' that gets produced in the target with energy $E_{A'} \equiv xE_0$ and decay at a distance z behind the front edge of the target is given by

$$\frac{dN}{dx dz} = N_e \frac{N_0 X_0}{A} \int_{E_{A'}}^{E_0} dE_1 \int_0^T dt I(E_1; E_0, t) \times \left(\frac{E_0}{E_1} \frac{d\sigma}{dx'} \right)_{x'=(E_{A'}/E_1)} \frac{dP(z - \frac{x_0}{\rho} t)}{dz}, \quad (\text{B1})$$

where E_0 is the incident energy, N_e the number of incident electrons, $N_0 = 6.02 \times 10^{23} \text{ mole}^{-1}$, ρ and X_0 are the density (in g/cm^3) and unit radiation length (in g/cm^2) of the target material, respectively, and

$$\frac{dP(\ell)}{d\ell} = \frac{1}{\ell_0} e^{-\ell/\ell_0} \quad (\text{B2})$$

is the differential decay probability where $\ell_0 \equiv \gamma c \tau = E_1 c \tau / m_{A'}$ is the A' decay length given in (12). Also,

$$I(E_1; E_0, t) \approx \begin{cases} \frac{1}{E_0} y^{bT-1} b t & T \gtrsim 1 \\ \delta(E_1 - E_0) & T \ll 1 \end{cases} \quad (\text{B3})$$

is the energy distribution of electrons at position t in the target, where $y \equiv \frac{E_0 - E_1}{E_0}$ and $b = 4/3$.

We can perform the t integration explicitly in the limit of a very thin or thick target ($T \ll 1$ or $T \gg 1$). For a thin target, we find

$$\frac{dN_{\text{thin}}}{dx dz} = N_e \frac{N_0 \rho \ell_0}{A} \frac{d\sigma}{dx} (e^{(T X_0 / \rho \ell_0)} - 1) \frac{dP(z)}{dz}. \quad (\text{B4})$$

For a thick target, we neglect the t dependence in the A' decay probability in (B1), since most production occurs within the first radiation length and thus well before the end of the dump. Here we find

$$\frac{dN_{\text{thick}}}{dx dz} \approx N_e \frac{N_0 X_0}{A} \int_{E_{A'}}^{E_0} dE_1 \tilde{I}(E_1; E_0, T) \times \left(\frac{E_0}{E_1} \frac{d\sigma}{dx'} \right)_{x'=(E_{A'}/E_1)} \frac{dP(z)}{dz}, \quad (\text{B5})$$

where

$$\tilde{I}(E_1; E_0, T) = \int_0^T dt I(E_1; E_0, t) \approx \frac{1 + y^{bT} (bT \ln y - 1)}{E_0 b y (\ln y)^2} \rightarrow \frac{1}{E_0 b y (\ln y)^2} \quad (\text{B6})$$

as $T \rightarrow \infty$. For finite T , the limiting form is a good approximation for small and moderate y , i.e. for electrons that carry a large fraction of the initial beam energy (for $y < 0.5$ and $T > 7$ it is correct to within 1%).

We note that by (8) and (B1), $\frac{1}{N_e} \frac{dN}{dx dz}$ is proportional to

$$\frac{1}{\ell_0} \frac{8\alpha^3 \epsilon^2 Z^2 \chi}{m_{A'}^2} \frac{N_0 X_0}{A}. \quad (\text{B7})$$

However, $\frac{1}{X_0} = (4\alpha^3 N_0 / m_e^2 A) [Z^2 (L_{\text{rad}} - f(Z)) + Z L'_{\text{rad}}]$, where L_{rad} , L'_{rad} , and f are logs set by the atomic form factors of the target atoms [49], and we obtain

$$\frac{dN}{dx dz} \sim \frac{\min(T, 1)}{\ell_0} \frac{m_e^2}{m_{A'}^2} \epsilon^2, \quad (\text{B8})$$

with only logarithmic dependence on the target nucleus Z . This expression has a simple physical interpretation: an electron is slowed in a radiation length by radiating a small number of relatively hard but collinear photons. The probability of instead radiating an A' is suppressed by the squared ratio of the couplings, ϵ^2 , and the squared ratio

of the masses $m_e^2/m_{A'}^2$, because it requires a higher invariant-mass intermediate state.

For decays at a given z , we applied an acceptance based on the detector geometry and energy cuts before integrating to obtain the expected total rate.

APPENDIX C: KINEMATICS OF SIGNAL AND CONTROLLING BACKGROUNDS

The dominant QED backgrounds for A' production are the trident reactions shown in Fig. 3. The γ^* process contributes an irreducible background to $A' \rightarrow l^+l^-$. The Bethe-Heitler process has a much larger rate, but can be controlled by exploiting its very different kinematics compared to the signal. Our aim in this appendix is to quantitatively describe the singularity structure of the Bethe-Heitler process and derive an effective set of cuts on lab-frame observables. Of course a more accurate basis for a final design would rely on Monte Carlo for these processes, but the simple calculation clarifies the origin of the large Bethe-Heitler cross section and how to regulate it by cutting away from the dangerous “forward” and “asymmetric” regions of phase space in the lab frame.

As an important reference, we will start by recalling the kinematic properties of A' production and decay using the results of Appendix A. We again consider a monochromatic incident electron beam of energy E_0 . Let θ_{cm} be the emission angle of the forward decay product relative to the A' direction in the A' rest frame. Let $\theta_{A'}$ be the emission angle of the A' relative to the beam direction in the lab frame. As we have shown, the characteristic A' emission angle is small and is set by $\theta_{A'} \sim \frac{m_{A'}\sqrt{1-x}}{E_0}$, where $x \equiv E_{A'}/E_0$. In the limit of small $\frac{m_{A'}}{xE_0}$, the lab-frame opening angles θ_{\pm} and energies E_{\pm} of the A' decay products are

$$E_{\pm} = \frac{xE_0}{2}(1 \pm \cos(\theta_{\text{cm}})), \quad (\text{C1})$$

$$\tan(\theta_{\pm}) = \pm \frac{1}{\gamma} \sqrt{\frac{1 \mp \cos(\theta_{\text{cm}})}{1 \pm \cos(\theta_{\text{cm}})}} + \tan(\theta_{A'}), \quad (\text{C2})$$

where $\gamma = \frac{xE_0}{m_{A'}}$.

The characteristic transverse momentum of the A' is $p_{A',\perp} \approx E_{A'}\theta_{A'} \sim \sqrt{1-x}m_{A'}$, while the typical recoil of the target is $|q_{\text{min}}| \approx (\frac{m_{A'}}{2xE_0})m_{A'}$. The median value of $1-x$ is $\overline{1-x} \approx \frac{m_{A'}}{E_0}$ for $m_{A'} \geq 50$ MeV, implying that $|q_{\text{min}}|$ is parametrically smaller than $p_{A',\perp}$ by $\sim \sqrt{\frac{m_{A'}}{E_0}}$. Evidently, the recoiling electron largely balances the recoil of the A' . The energy E_R and angle θ_R of the recoiling final-state beam electron in the laboratory frame are

$$E_R = (1-x)E_0 \approx m_{A'}, \quad (\text{C3})$$

$$\tan(\theta_R) \approx \sqrt{\frac{m_{A'}}{E_0}} \left(1 + \frac{m_{A'}}{2E_0} + \dots\right). \quad (\text{C4})$$

Note the relatively wide angle of the recoiling electron relative to the A' decay products. Equations (C1)–(C4) summarize the important kinematic characteristics of A' production.

As with A' production, trident reactions can also be analyzed using the Weizsäcker-Williams approximation, where we group an outgoing l^+l^- pair with fixed invariant mass m^2 to act as the A' candidate. In the case of Bethe-Heitler production, we can further approximate the beam electron as splitting at small angle into the recoil electron and a nearly on-shell photon, which scatters with the Coulomb photon into the l^+l^- pair (see Fig. 11). There are two sources of large logs in the Bethe-Heitler cross section: the soft and collinear logs in the photon radiation by the electron and a forward-scattering log in the $\gamma\gamma \rightarrow l^+l^-$ subprocess. Both are regulated by m_e , and can be further suppressed by kinematic requirements. We postpone the derivation—a matter of standard results and kinematic bookkeeping—to the following section, and focus here on its implications.

In this approximation, upon integrating over an invariant-mass window of size δm about $m_{A'}$, we find

$$\frac{d\sigma}{dx d\cos\theta_{A'} d\hat{c}} = \frac{2\alpha^4 \chi}{\pi} \frac{\delta m}{m_{A'}} \frac{1}{m_{A'}^2} \frac{1 + (1-x)^2}{\theta_{A'}^2 x} \times \left(\frac{1 + \hat{c}}{1 - \hat{c}} + \frac{1 - \hat{c}}{1 + \hat{c}} \right), \quad (\text{C5})$$

where x and $\theta_{A'}$ are defined as before, and $\hat{c} = \cos\theta_{\text{cm}}$, where θ_{cm} is measured relative to the axis of the incoming photons in the $\gamma\gamma \rightarrow l^+l^-$ process, which is near enough to the beam axis for our purposes. This displays the expected singularities at small x (soft), $|\hat{c}| \rightarrow 1$ (forward scattering), and small $\theta_{A'}$ (collinear). This is quite different behavior from the signal and radiative backgrounds, which are peaked at large values of x and slowly varying in \hat{c} .

Requiring x above $1 - \delta$, with δ near or below its median value $\bar{\delta} = \max(m_{A'}/E_0, m_e/m_{A'})$, keeps a large fraction of the signal and suppresses the Bethe-Heitler background by a factor of δ . Likewise, the signal is relatively flat in $\hat{c} = \cos\theta_{\text{cm}}$. According to (C1) and (C2), we can ensure modest \hat{c} by constraining the ratio of the lab-

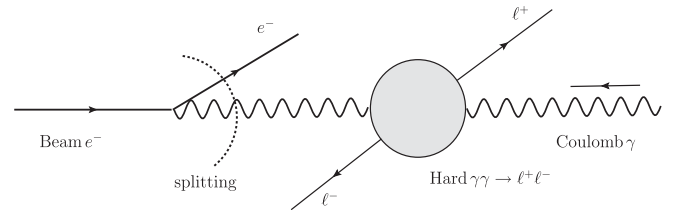


FIG. 11. Bethe-Heitler reactions viewed as hard $\gamma\gamma \rightarrow l^+l^-$ processes.

frame energies or of the opening angles of the two decay products to be near unity.

There remains the collinear singularity at small $\theta_{A'}$. The signal is also peaked forward, but with a singularity regulated by $m_{A'}$ rather than m_e , so that it is produced at much wider characteristic A' angles than Bethe-Heitler processes. Since the absolute angles $\sim(m_{A'}/E_0)^{3/2}$ are still small and must be obtained by summing two momenta, it is impractical to place a lower bound on the A' emission angle. It is probably much easier to cut on the angle θ_R of the recoiling electron. Since the recoiling electron has much lower energy at large x and approximately balances the transverse momentum of the A' , it is emitted at a much larger angle. For the median x , the electron energy $\sim m_{A'}$ and its angle $\sim(m_{A'}/E_0)^{1/2}$. Requiring the recoiling electron momentum and angle near these values significantly reduces the Bethe-Heitler rate. In a similar spirit, it may or may not also be easier to implement a tight x cut using the energy of the recoil electron rather than the total energy of the decay products making up the A' candidate. After these cuts, we find

$$\begin{aligned} \sigma_{\text{cut}}(x_{\min}, \theta_{R,\min}, |\hat{c}|_{\max}) & \\ & \approx \frac{16\alpha^4 \chi}{\pi} \frac{\delta m}{m_{A'}} \frac{1}{m_{A'}^2} \log((1-x_{\min})^{-1} \theta_{R,\min}^{-1}) \\ & \quad \times (1-x_{\min})(\tanh^{-1}|\hat{c}|_{\max} - |\hat{c}|_{\max}/2). \end{aligned} \quad (\text{C6})$$

When θ_{cut} is small relative to the typical angular spread $\frac{m_{A'}}{E_0}(1-x)$ of the signal and radiative backgrounds, the factor on the first line is related to the lepton-pair cross section σ_{rad} with the same cuts from the radiative diagrams alone by

$$9\sigma_{\text{rad}}\left(\log\frac{1-x_{\min}}{1-x_{\max}}\right)^{-1} \epsilon_{\text{rad}}^{-1}(\theta_{R,\min}, |\hat{c}|_{\max}), \quad (\text{C7})$$

where $1-x_{\max} = \max(m_A^2/E_0^2, m_e^2/m_A^2)$ is the value of x where the log divergence in σ_{rad} is regulated, and ϵ_{rad} the efficiency for the radiative process (or signal) to pass θ_R and $|\hat{c}|$ selections.

Let us consider a representative case, $E_0 = 5$ GeV, $m_{A'} = 0.5$ GeV. Requiring $x > 0.9$, $\theta_R > 1/10$, and $E_+/E_- < 3$ (i.e. $\hat{c} < 0.5$), we retain roughly 20% of the signal and reduce the contribution of Bethe-Heitler to the signal region to roughly the same size as the radiative contribution. A proper optimization of these cuts is best done with full Monte Carlo for the background, and of course depends on the characteristics of an individual experiment, but we have confirmed numerically that the kinematic differences between Bethe-Heitler and radiative production are sufficient that it can be made subdominant while maintaining high efficiency for the A' signal.

In the case of $A' \rightarrow e^+e^-$, the Bethe-Heitler process can also contribute with the electron labeled ℓ^- in Fig. 3 identified as the recoiler and ℓ^+ and e^- forming the A' candidate. Here the recoil electron kinematics is as in the

signal process but there is a forward-scattering singularity when most of the A' -candidate energy is carried by the e^- with a softer e^+ . The cuts above remove this singularity as well, and we will not discuss it further.

1. Bethe-Heitler pair production in the collinear splitting approximation

We now extend the earlier Weizsäcker-Williams treatment to compute the Bethe-Heitler pair production cross section. Using the notation defined in Appendix A, but now with an outgoing lepton/antilepton pair with momenta l^-/l^+ , the fully differential cross section is

$$\begin{aligned} \frac{d\sigma(p_1 + P_i \rightarrow p_2 + l^+ + l^- + P_f)}{dE_{A'} d\cos\theta_{A'} dm^2 d\hat{t} d\phi_d} & \\ = \left(\frac{\alpha\chi}{\pi}\right) \left(\frac{E_0 x \beta_{A'}}{(1-x)}\right) \frac{d\sigma(p_1 + q \rightarrow p_2 + l^+ + l^-)}{d(p_1 \cdot a) dm^2 d\hat{t} d\phi_d} \Big|_{t=t_{\min}}, & \end{aligned} \quad (\text{C8})$$

where $a = l^+ + l^-$ is the total four-momentum of the A' candidate, $m^2 = a^2$ its invariant mass, and $\hat{t} = (l^+ - q)^2 = (l^+ - P_f + P_i)^2$. ϕ_d is the angle between p_1 and l^+ in the rest frame of a . As before, the hard subprocesses ($2 \rightarrow 3$ in this case) are separated from the soft Coulomb photon exchange.

Starting from Eq. (C8), we will analyze the behavior of Bethe-Heitler reactions [see Fig. 3(b)] relative to A' production in a leading logarithm approximation. This suffices to identify the singularities.

To write the right-hand side of (C8) in the approximation of near-collinear splitting, it is useful to introduce the more familiar z and p_{\perp} variables and relate them to the kinematic variables in the center-of-mass frame of the beam electron and Coulomb photon and to the lab frame. We recall that in the lab frame, the Coulomb photon is purely spacelike, with $|\vec{q}| = \sqrt{t_{\min}} = \frac{U(x, \theta_{A'})}{2E_0(1-x)} \approx m^2/(2E_0x)$ for small $\theta_{A'}$ (we have replaced $m_{A'}^2$ with the invariant mass m^2 for the off-shell processes, but the kinematic conditions are unchanged). As $|\vec{q}|$ at t_{\min} kinematics depends on x and $\theta_{A'}$, the center-of-mass frame does too—it is obtained from the center-of-mass frame by boosting with $\beta \approx 1 - q/E_0$ (we drop much smaller $\theta_{A'}$ -dependent corrections), leading to center-of-mass-frame momenta for the incoming electron and Coulomb photon,

$$p_1^{\text{cm}} = (p, 0, 0, p), \quad (\text{C9})$$

$$q^{\text{cm}} = (\beta p, 0, 0, -p), \quad (\text{C10})$$

where $p = \sqrt{\frac{qE}{2(1-q/E)}}$. The recoil electron has momentum

$$p_2^{\text{lab}} = \left((1-x)E_0, E_0\theta_{A'}x, 0, (1-x)E_0 - \frac{E_0\theta_{A'}^2x^2}{2(1-x)} \right), \quad (\text{C11})$$

$$p_2^{\text{cm}} = (zp, p_{\perp}, 0, \sqrt{z^2 p^2 - p_{\perp}^2}), \quad (\text{C12})$$

where

$$z \equiv 1 - x, \quad p_{\perp} \equiv E_0 \theta_{A'} x, \quad (\text{C13})$$

up to corrections of higher order in $\theta_{A'}$ and m_e . For small p_{\perp} , we can now approximate

$$\frac{d\sigma}{dz dp_{\perp}^2 d\hat{t} d\phi_d} = \left(\frac{\alpha}{2\pi}\right) \frac{[1 + z^2]}{(1 - z)p_{\perp}^2} \frac{d\sigma(\gamma\gamma \rightarrow l^+ l^-)}{d\hat{t} d\phi_d}, \quad (\text{C14})$$

where

$$\frac{d\sigma(\gamma\gamma \rightarrow l^+ l^-)}{d\hat{t} d\phi_d} = \frac{\alpha^2}{m^4} \left(\frac{\hat{t}}{\hat{u}} + \frac{\hat{u}}{\hat{t}} \right). \quad (\text{C15})$$

We emphasize that the recoil electron is always right-moving, so the splitting approximation is valid where the Bethe-Heitler cross section is largest, but is never a good approximation for the radiative (or signal) processes, where the $\gamma^* \rightarrow e^- e^{+*}$ ‘‘splitting’’ always produces an electron going backwards relative to the γ^* .

The kinematic variables of (C8) are related to z, p_{\perp}, ϕ_d by

$$m^2 = a^2 = (1 + \beta - 2z)(1 + \beta)p^2, \quad (\text{C16})$$

$$p_{1,a} = (1 + \beta - z)p^2 + zp^2 \sqrt{1 - \frac{p_{\perp}^2}{z^2 p^2}}, \quad (\text{C17})$$

$$\phi_d = \phi_a, \quad (\text{C18})$$

leading to a Jacobian factor

$$\frac{d^2}{d(p_{1,a}) dm^2} \approx \frac{z}{p^2(1 + \beta)} \frac{d^2}{dp_{\perp}^2 dz} \approx \frac{2x(1 - x)}{m^2} \frac{d^2}{dp_{\perp}^2 dz}. \quad (\text{C19})$$

Taking $1 + \beta \rightarrow 2, p^2 \rightarrow \frac{|\vec{q}|E_0}{2} \approx \frac{m^2}{4x}$, we find

$$\begin{aligned} & \frac{d\sigma(p_1 + q \rightarrow p_2 + l^+ + l^-)}{d(p_{1,a}) dm^2 d\hat{t} d\phi_d} \Big|_{t=t_{\min}(x, \theta_{A'})} \\ &= \frac{\alpha}{2\pi} \frac{1 + (1 - x)^2}{E_0^2 \theta_{A'}^2 x^3} \frac{2x(1 - x)}{m^2} \frac{\alpha^2}{m^4} \left(\frac{\hat{t}}{\hat{u}} + \frac{\hat{u}}{\hat{t}} \right), \end{aligned} \quad (\text{C20})$$

and hence by (C8),

$$\frac{d\sigma}{dx d\cos\theta_{A'} dm^2 d\hat{t} d\phi_d} = \frac{\alpha^4 \chi}{\pi^2} \frac{1 + (1 - x)^2}{\theta_{A'}^2 x} \frac{1}{m^6} \left(\frac{\hat{t}}{\hat{u}} + \frac{\hat{u}}{\hat{t}} \right). \quad (\text{C21})$$

Changing variables from \hat{t} to $\hat{c} = \cos\theta_{\text{cm}}$ of the $2 \rightarrow 2$ process, $\hat{t} = \frac{m^2}{2}(1 - \hat{c})$, and integrating over ϕ_d and over m^2 from $m_{A'}^2 - m_{A'} \delta m$ to $m_{A'}^2 + m_{A'} \delta m$, we obtain the result of Eq. (C5).

-
- [1] B. Holdom, Phys. Lett. **166B**, 196 (1986).
[2] K. R. Dienes, C. F. Kolda, and J. March-Russell, Nucl. Phys. **B492**, 104 (1997).
[3] S. A. Abel and B. W. Schofield, Nucl. Phys. **B685**, 150 (2004).
[4] S. A. Abel, M. D. Goodsell, J. Jaeckel, V. V. Khoze, and A. Ringwald, J. High Energy Phys. 07 (2008) 124.
[5] A. Ringwald, arXiv:0810.3106.
[6] N. Arkani-Hamed and N. Weiner, J. High Energy Phys. 12 (2008) 104.
[7] C. Cheung, J. T. Ruderman, L.-T. Wang, and I. Yavin, Phys. Rev. D **80**, 035008 (2009).
[8] D. E. Morrissey, D. Poland, and K. M. Zurek, J. High Energy Phys. 07 (2009) 050.
[9] A. Katz and R. Sundrum, J. High Energy Phys. 06 (2009) 003.
[10] M. Baumgart, C. Cheung, J. T. Ruderman, L.-T. Wang, and I. Yavin, J. High Energy Phys. 04 (2009) 014.
[11] O. Adriani *et al.*, Nature (London) **458**, 607 (2009).
[12] J. Chang *et al.*, Nature (London) **456**, 362 (2008).
[13] A. A. Abdo *et al.* (Fermi LAT), Phys. Rev. Lett. **102**, 181101 (2009).
[14] F. Aharonian *et al.* (H.E.S.S.), Phys. Rev. Lett. **101**, 261104 (2008).
[15] C. F. Aharonian (H.E.S.S.), arXiv:0905.0105.
[16] N. Arkani-Hamed, D. P. Finkbeiner, T. R. Slatyer, and N. Weiner, Phys. Rev. D **79**, 015014 (2009).
[17] M. Pospelov and A. Ritz, Phys. Lett. B **671**, 391 (2009).
[18] J. Hisano, S. Matsumoto, and M. M. Nojiri, Phys. Rev. Lett. **92**, 031303 (2004).
[19] J. March-Russell, S. M. West, D. Cumberbatch, and D. Hooper, J. High Energy Phys. 07 (2008) 058.
[20] M. Cirelli, M. Kadastik, M. Raidal, and A. Strumia, Nucl. Phys. **B813**, 1 (2009).
[21] I. Cholis, G. Dobler, D. P. Finkbeiner, L. Goodenough, and N. Weiner, arXiv:0811.3641.
[22] I. Cholis, D. P. Finkbeiner, L. Goodenough, and N. Weiner, arXiv:0810.5344.
[23] Y. Cui, D. E. Morrissey, D. Poland, and L. Randall, J. High Energy Phys. 05 (2009) 076.
[24] D. Tucker-Smith and N. Weiner, Phys. Rev. D **64**, 043502 (2001).
[25] R. Bernabei *et al.*, Int. J. Mod. Phys. D **13**, 2127 (2004).
[26] R. Bernabei *et al.* (DAMA), Eur. Phys. J. C **56**, 333 (2008).
[27] S. Chang, G. D. Kribs, D. Tucker-Smith, and N. Weiner,

- Phys. Rev. D **79**, 043513 (2009).
- [28] D. Alves, S. R. Behbahani, P. Schuster, and J. G. Wacker, arXiv:0903.3945.
- [29] C.-R. Chen, F. Takahashi, and T. T. Yanagida, Phys. Lett. B **673**, 255 (2009).
- [30] C.-R. Chen, M. M. Nojiri, F. Takahashi, and T. T. Yanagida, Prog. Theor. Phys. **122**, 553 (2009).
- [31] S. Shirai, F. Takahashi, and T. T. Yanagida, Phys. Lett. B **675**, 73 (2009).
- [32] A. Ibarra, A. Ringwald, D. Tran, and C. Weniger, J. Cosmol. Astropart. Phys. **08** (2009) 017.
- [33] S. Shirai, F. Takahashi, and T. T. Yanagida, arXiv:0905.3235.
- [34] R. Essig, N. Sehgal, and L. E. Strigari, Phys. Rev. D **80**, 023506 (2009).
- [35] A. Arvanitaki *et al.*, Phys. Rev. D **79**, 105022 (2009).
- [36] B. Majorovits *et al.*, arXiv:astro-ph/0411396.
- [37] J. Angle *et al.* (XENON), Phys. Rev. Lett. **100**, 021303 (2008).
- [38] R. Hasty (XENON), AIP Conf. Proc. **842**, 992 (2006).
- [39] L. W. Kastens, S. B. Cahn, A. Manzur, and D. N. McKinsey, arXiv:0905.1766.
- [40] D. P. Finkbeiner, T. Lin, and N. Weiner, arXiv:0906.0002.
- [41] R. Essig, P. Schuster, and N. Toro, Phys. Rev. D **80**, 015003 (2009).
- [42] B. Batell, M. Pospelov, and A. Ritz, Phys. Rev. D **79**, 115008 (2009).
- [43] M. Reece and L.-T. Wang, J. High Energy Phys. **07** (2009) 051.
- [44] F. Bossi, arXiv:0904.3815.
- [45] P.-f. Yin, J. Liu, and S.-h. Zhu, Phys. Lett. B **679**, 362 (2009).
- [46] K. J. Kim and Y.-S. Tsai, Phys. Rev. D **8**, 3109 (1973).
- [47] Y.-S. Tsai, Rev. Mod. Phys. **46**, 815 (1974).
- [48] Y.-S. Tsai, Phys. Rev. D **34**, 1326 (1986).
- [49] C. Amsler *et al.* (Particle Data Group), Phys. Lett. B **667**, 1 (2008).
- [50] B. Aubert *et al.* (BABAR), arXiv:0902.2176.
- [51] M. Pospelov, arXiv:0811.1030.
- [52] J. D. Bjorken *et al.*, Phys. Rev. D **38**, 3375 (1988).
- [53] E. M. Riordan *et al.*, Phys. Rev. Lett. **59**, 755 (1987).
- [54] A. Bross *et al.*, Phys. Rev. Lett. **67**, 2942 (1991).
- [55] M. S. Turner, Phys. Rev. Lett. **60**, 1797 (1988).
- [56] N. Iwamoto, Phys. Rev. Lett. **53**, 1198 (1984).
- [57] A. A. Prinz *et al.*, Phys. Rev. Lett. **81**, 1175 (1998).
- [58] F. Bergsma *et al.* (CHARM), Phys. Lett. B **157**, 458 (1985).
- [59] B. A. Mecking *et al.* (CLAS), Nucl. Instrum. Methods Phys. Res., Sect. A **503**, 513 (2003).
- [60] A. Afanasev *et al.*, Phys. Lett. B **679**, 317 (2009).
- [61] A. Afanasev *et al.*, Phys. Rev. Lett. **101**, 120401 (2008).
- [62] M. Ahlers, H. Gies, J. Jaeckel, J. Redondo, and A. Ringwald, Phys. Rev. D **76**, 115005 (2007).
- [63] J. Jaeckel and A. Ringwald, Phys. Lett. B **659**, 509 (2008).
- [64] M. Ahlers, H. Gies, J. Jaeckel, J. Redondo, and A. Ringwald, Phys. Rev. D **77**, 095001 (2008).
- [65] J. Jaeckel and J. Redondo, Europhys. Lett. **84**, 31 002 (2008).
- [66] M. Ahlers, J. Jaeckel, J. Redondo, and A. Ringwald, Phys. Rev. D **78**, 075005 (2008).
- [67] M. Fouche *et al.*, Phys. Rev. D **78**, 032013 (2008).
- [68] K. Ehret *et al.*, arXiv:0905.4159.
- [69] D. Hooper and T. M. P. Tait, Phys. Rev. D **80**, 055028 (2009).
- [70] J. Mardon, Y. Nomura, and J. Thaler, Phys. Rev. D **80**, 035013 (2009).
- [71] Y. Nomura and J. Thaler, Phys. Rev. D **79**, 075008 (2009).
- [72] M. J. Strassler and K. M. Zurek, Phys. Lett. B **651**, 374 (2007).
- [73] M. J. Strassler, arXiv:0801.0629.